

Exciton-Plasmon Interactions in Individual Carbon Nanotubes¹

Igor V. Bondarev

*Department of Physics, North Carolina Central University
Durham, NC 27707, USA*

E-mail: ibondarev@ncsu.edu

Lilia M. Woods and Adrian Popescu

*Department of Physics, University of South Florida
Tampa, FL 33620, USA*

We use the macroscopic quantum electrodynamics approach suitable for absorbing and dispersing media to study the properties and role of collective surface excitations — excitons and plasmons — in single-wall and double-wall carbon nanotubes. We show that the interactions of excitonic states with surface electromagnetic modes in individual small-diameter ($\lesssim 1$ nm) single-walled carbon nanotubes can result in strong exciton-surface-plasmon coupling. Optical response of individual nanotubes exhibits Rabi splitting ~ 0.1 eV, both in the linear excitation regime and in the non-linear excitation regime with the photoinduced biexcitonic states formation, as the exciton energy is tuned to the nearest interband surface plasmon resonance of the nanotube. An electrostatic field applied perpendicular to the nanotube axis can be used to control the exciton-plasmon coupling. For double-wall carbon nanotubes, we show that at tube separations similar to their equilibrium distances interband surface plasmons have a profound effect on the inter-tube Casimir force. Strong overlapping plasmon resonances from both tubes warrant their stronger attraction. Nanotube chiralities possessing such collective excitation features will result in forming the most favorable inner-outer tube combination in double-wall carbon nanotubes. These results pave the way for the development of new generation of tunable optoelectronic and nano-electromechanical device applications with carbon nanotubes.

Keywords: Carbon nanotubes, Near-field effects, Excitons, Plasmons

¹To appear in "Plasmons: Theory and Applications", ed. K.Helsey (Nova Publishers, NY, USA)

1 Introduction

Single-walled carbon nanotubes (CNs) are quasi-one-dimensional (1D) cylindrical wires consisting of graphene sheets rolled-up into cylinders with diameters $\sim 1 - 10$ nm and lengths $\sim 1 - 10^4$ μm [1, 2, 3, 4]. CNs are shown to be useful as miniaturized electronic, electromechanical, and chemical devices [5], scanning probe devices [6], and nanomaterials for macroscopic composites [7]. The area of their potential applications was recently expanded to nanophotonics [8, 9, 10, 11, 12, 13] after the demonstration of controllable single-atom incapsulation into CNs [14, 15, 16, 17], and even to quantum cryptography since the experimental evidence was reported for quantum correlations in the photoluminescence spectra of individual nanotubes [18].

For pristine (undoped) single-walled CNs, the numerical calculations predicting large exciton binding energies ($\sim 0.3-0.6$ eV) in semiconducting CNs [19, 20, 21] and even in some small-diameter (~ 0.5 nm) metallic CNs [22], followed by the results of various exciton photoluminescence measurements [18, 23, 24, 25, 26, 27], have become available. These works, together with other reports investigating the role of effects such as intrinsic defects [25, 28], exciton-phonon interactions [26, 28, 29, 30, 31], biexciton formation [32, 33], exciton-surface-plasmon coupling [34, 35, 36, 37], external magnetic [38, 39] and electric fields [37, 40], reveal the variety and complexity of the intrinsic optical properties of CNs [41].

Carbon nanotubes combine advantages such as electrical conductivity, chemical stability, high surface area, and unique optoelectronic properties that make them excellent potential candidates for a variety of applications, including efficient solar energy conversion [7], energy storage [14], optical nanobiosensorics [42]. However, the quantum yield of individual CNs is normally very low. Nanotube composites of CN bundles and/or films could surpass this difficulty, opening up new paths for the development of high-yield, high-performance optoelectronics applications with CNs [43, 44]. Understanding the inter-tube interactions is important in order to be able to tailor properties of CN bundles and films, as well as properties of multi-wall CNs. This is also important for experimental realization of new effects and devices proposed recently, such as trapping of cold atoms [42, 45] and their entanglement [11] near single-walled CNs, surface profiling [6] and nanolithography applications [46] with double-wall CNs.

Here, we use the macroscopic Quantum ElectroDynamics (QED) formalism developed earlier for absorbing and dispersive media [47, 48, 49, 9] and then successfully employed to study near-field EM effects in hybrid CN systems [10, 11, 45], to investigate the properties and role of collective surface excitations — excitons and plasmons — in single-wall and double-wall CNs. First, we show that, due to the presence of low-energy ($\sim 0.5-2$ eV) weakly-dispersive interband plasmon modes [50] and large exciton excitation energies in the same energy domain [51, 52], the excitons can form strongly coupled mixed exciton-plasmon excitations in indi-

vidual small-diameter ($\lesssim 1$ nm) semiconducting single-walled CNs. The exciton-plasmon coupling (and the exciton emission accordingly) can be controlled by an external electrostatic field applied perpendicular to the CN axis (the quantum confined Stark effect). The optical response of individual CNs exhibits the Rabi splitting of ~ 0.1 eV, both in the linear excitation regime and in the non-linear excitation regime with the photoinduced biexcitonic states formation, as the exciton energy is tuned to the nearest interband surface plasmon resonance of the CN. Previous studies of the exciton-plasmon coupling have been focused on artificially fabricated *hybrid* plasmonic nanostructures, such as dye molecules in organic polymers deposited on metallic films [53], semiconductor quantum dots coupled to metallic nanoparticles [54], or nanowires [55], where semiconductor material carries the exciton and metal carries the plasmon. Our results are particularly interesting since they reveal the fundamental electromagnetic (EM) phenomenon — the strong exciton-plasmon coupling — in an *individual* quasi-1D nanostructure, a carbon nanotube, as well as its tunability feature by means of the quantum confined Stark effect. We expect these results to open up new paths for the development of tunable optoelectronic device applications with optically excited carbon nanotubes, including the strong excitation regime with optical non-linearities.

Next, we turn to the double-wall carbon nanotubes to investigate the effect of collective surface excitations on the inter-tube Casimir interaction in these systems. The Casimir interaction is a paradigm for a force induced by quantum EM fluctuations. The fundamental nature of this force has been studied extensively ever since the prediction of the existence of an attraction between neutral metallic mirrors in vacuum [49, 56]. In recent years, the Casimir effect has acquired a much broader impact due to its importance for nanostructured materials and devices. The development and operation of micro- and nano-electromechanical systems are limited due to unwanted effects, such as stiction, friction, and adhesion, originating from the Casimir force [57]. This interaction is also an important component for the stability of nanomaterials. Here, we show that at tube separations similar to their equilibrium distances interband surface plasmons have a profound effect on the inter-tube Casimir force. Strong overlapping plasmon resonances from both tubes warrant their stronger attraction. Nanotube chiralities possessing such collective excitation features will result in forming the most favorable inner-outer tube combination in double-wall carbon nanotubes. This theoretical understanding is important for the development of nano-electromechanical devices with CNs.

This Chapter is organized as follows. Section 2 introduces the general Hamiltonian of the exciton interaction with vacuum-type quantized surface EM modes of a single-walled CN. No external EM field is assumed to be applied. The vacuum-type-field we consider is created by CN surface EM fluctuations. Section 3 explains how the interaction introduced results in the coupling of the excitonic states to the nanotube's surface plasmon modes. Here we derive and discuss the characteristics of the coupled exciton-plasmon excitations, such as the dispersion relation,

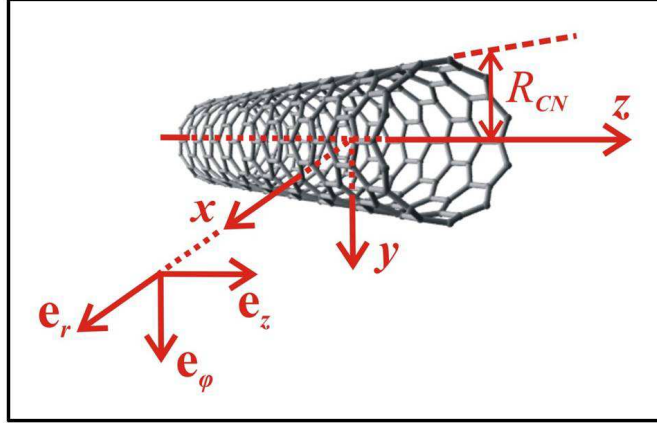


Figure 1: The geometry of the problem.

the plasmon density of states (DOS), and the optical response functions, for particular semiconducting CNs of different diameters. We also analyze how the electrostatic field applied perpendicular to the CN axis affects the CN band gap, the exciton binding energy, and the surface plasmon energy, to explore the tunability of the exciton-surface-plasmon coupling in CNs. Section 4 derives and analyzes the Casimir interaction between two concentric cylindrical graphene sheets comprising a double-wall CN. The summary and conclusions of the work are given in Sec. 5. All the technical details about the construction and diagonalization of the exciton-field Hamiltonian, the EM field Green tensor derivation, the perpendicular electrostatic field effect, are presented in the Appendices in order not to interrupt the flow of the arguments and results.

2 Exciton-electromagnetic-field interaction on the nanotube surface

We consider the vacuum-type EM interaction of an exciton with the quantized surface electromagnetic fluctuations of a single-walled semiconducting CN by using our recently developed Green function formalism to quantize the EM field in the presence of quasi-1D absorbing bodies [58, 59, 60, 61, 62, 9]. No external EM field is assumed to be applied. The nanotube is modelled by an infinitely thin, infinitely long, anisotropically conducting cylinder with its surface conductivity obtained from the realistic band structure of a particular CN. Since the problem has the cylindrical symmetry, the orthonormal cylindrical basis $\{\mathbf{e}_r, \mathbf{e}_\varphi, \mathbf{e}_z\}$ is used with the vector \mathbf{e}_z directed along the nanotube axis as shown in Fig. 1. Only the axial conductivity, σ_{zz} , is taken into account, whereas the azimuthal one, $\sigma_{\varphi\varphi}$, being strongly suppressed by the transverse depolarization effect [63, 64, 65, 66, 67, 68], is neglected.

The total Hamiltonian of the coupled exciton-photon system on the nanotube surface is of the form

$$\hat{H} = \hat{H}_F + \hat{H}_{ex} + \hat{H}_{int}, \quad (1)$$

where the three terms represent the free (medium-assisted) EM field, the free (non-interacting) exciton, and their interaction, respectively. More explicitly, the second quantized field Hamiltonian is

$$\hat{H}_F = \sum_{\mathbf{n}} \int_0^{\infty} d\omega \hbar\omega \hat{f}^\dagger(\mathbf{n}, \omega) \hat{f}(\mathbf{n}, \omega), \quad (2)$$

where the scalar bosonic field operators $\hat{f}^\dagger(\mathbf{n}, \omega)$ and $\hat{f}(\mathbf{n}, \omega)$ create and annihilate, respectively, the surface EM excitation of frequency ω at an arbitrary point $\mathbf{n} = \mathbf{R}_n = \{R_{CN}, \varphi_n, z_n\}$ associated with a carbon atom (representing a lattice site – Fig. 1) on the surface of the CN of radius R_{CN} . The summation is made over all the carbon atoms, and in the following it is replaced by the integration over the entire nanotube surface according to the rule

$$\sum_{\mathbf{n}} \dots = \frac{1}{S_0} \int d\mathbf{R}_n \dots = \frac{1}{S_0} \int_0^{2\pi} d\varphi_n R_{CN} \int_{-\infty}^{\infty} dz_n \dots, \quad (3)$$

where $S_0 = (3\sqrt{3}/4)b^2$ is the area of an elementary equilateral triangle selected around each carbon atom in a way to cover the entire surface of the nanotube, $b = 1.42 \text{ \AA}$ is the carbon-carbon interatomic distance.

The second quantized Hamiltonian of the free exciton (see, e.g., Ref. [69]) on the CN surface is of the form

$$\hat{H}_{ex} = \sum_{\mathbf{n}, \mathbf{m}, f} E_f(\mathbf{n}) B_{\mathbf{n}+\mathbf{m}, f}^\dagger B_{\mathbf{m}, f} = \sum_{\mathbf{k}, f} E_f(\mathbf{k}) B_{\mathbf{k}, f}^\dagger B_{\mathbf{k}, f}, \quad (4)$$

where the operators $B_{\mathbf{n}, f}^\dagger$ and $B_{\mathbf{n}, f}$ create and annihilate, respectively, an exciton with the energy $E_f(\mathbf{n})$ in the lattice site \mathbf{n} of the CN surface. The index $f (\neq 0)$ refers to the internal degrees of freedom of the exciton. Alternatively,

$$B_{\mathbf{k}, f}^\dagger = \frac{1}{\sqrt{N}} \sum_{\mathbf{n}} B_{\mathbf{n}, f}^\dagger e^{i\mathbf{k}\cdot\mathbf{n}} \quad \text{and} \quad B_{\mathbf{k}, f} = (B_{\mathbf{k}, f}^\dagger)^\dagger \quad (5)$$

create and annihilate the f -internal-state exciton with the quasi-momentum $\mathbf{k} = \{k_\varphi, k_z\}$, where the azimuthal component is quantized due to the transverse confinement effect and the longitudinal one is continuous, N is the total number of the lattice sites (carbon atoms) on the CN surface. The exciton total energy is then written in the form

$$E_f(\mathbf{k}) = E_{ex}^{(f)}(k_\varphi) + \frac{\hbar^2 k_z^2}{2M_{ex}(k_\varphi)} \quad (6)$$

Here, the first term represents the excitation energy

$$E_{exc}^{(f)}(k_\varphi) = E_g(k_\varphi) + E_b^{(f)}(k_\varphi) \quad (7)$$

of the f -internal-state exciton with the (negative) binding energy $E_b^{(f)}$, created via the interband transition with the band gap

$$E_g(k_\varphi) = \varepsilon_e(k_\varphi) + \varepsilon_h(k_\varphi), \quad (8)$$

where $\varepsilon_{e,h}$ are transversely quantized azimuthal electron-hole subbands (see the schematic in Fig. 2). The second term in Eq. (6) represents the kinetic energy of the translational longitudinal movement of the exciton with the effective mass $M_{ex} = m_e + m_h$, where m_e and m_h are the (subband-dependent) electron and hole effective masses, respectively. The two equivalent free-exciton Hamiltonian representations are related to one another via the obvious orthogonality relationships

$$\frac{1}{N} \sum_{\mathbf{n}} e^{-i(\mathbf{k}-\mathbf{k}')\cdot\mathbf{n}} = \delta_{\mathbf{k}\mathbf{k}'}, \quad \frac{1}{N} \sum_{\mathbf{k}} e^{-i(\mathbf{n}-\mathbf{m})\cdot\mathbf{k}} = \delta_{\mathbf{n}\mathbf{m}} \quad (9)$$

with the \mathbf{k} -summation running over the first Brillouin zone of the nanotube. The bosonic field operators in \hat{H}_F are transformed to the \mathbf{k} -representation in the same way.

The most general (non-relativistic, electric dipole) exciton-photon interaction on the nanotube surface can be written in the form (we use the Gaussian system of units and the Coulomb gauge; see details in Appendix A)

$$\hat{H}_{int} = \sum_{\mathbf{n}, \mathbf{m}, f} \int_0^\infty d\omega [g_f^{(+)}(\mathbf{n}, \mathbf{m}, \omega) B_{\mathbf{n}, f}^\dagger - g_f^{(-)}(\mathbf{n}, \mathbf{m}, \omega) B_{\mathbf{n}, f}] \hat{f}(\mathbf{m}, \omega) + h.c., \quad (10)$$

where

$$g_f^{(\pm)}(\mathbf{n}, \mathbf{m}, \omega) = g_f^\perp(\mathbf{n}, \mathbf{m}, \omega) \pm \frac{\omega}{\omega_f} g_f^\parallel(\mathbf{n}, \mathbf{m}, \omega) \quad (11)$$

with

$$g_f^{\perp(\parallel)}(\mathbf{n}, \mathbf{m}, \omega) = -i \frac{4\omega_f}{c^2} \sqrt{\pi \hbar \omega \operatorname{Re} \sigma_{zz}(R_{CN}, \omega)} (\mathbf{d}_{\mathbf{n}}^f)_z{}^{\perp(\parallel)} G_{zz}(\mathbf{n}, \mathbf{m}, \omega) \quad (12)$$

being the interaction matrix element where the exciton with the energy $E_{exc}^{(f)} = \hbar\omega_f$ is excited through the electric dipole transition $(\mathbf{d}_{\mathbf{n}}^f)_z = \langle 0 | (\hat{\mathbf{d}}_{\mathbf{n}})_z | f \rangle$ in the lattice site \mathbf{n} by the nanotube's transversely (longitudinally) polarized surface EM modes. The modes are represented in the matrix element by the transverse (longitudinal) part of the Green tensor zz -component $G_{zz}(\mathbf{n}, \mathbf{m}, \omega)$ of the EM subsystem (Appendix B). This is the only Green tensor component we have to take into account. All the other components can be safely neglected as they are greatly suppressed by the strong transverse depolarization effect in CNs [63, 64, 65, 66, 67, 68]. As a consequence,

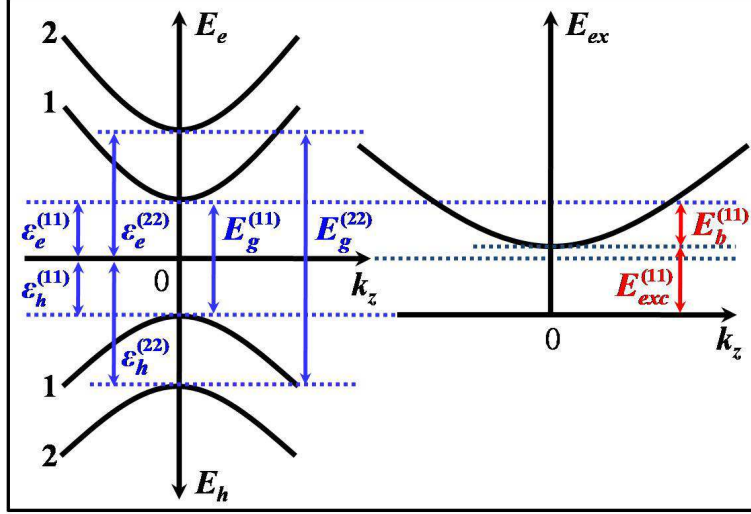


Figure 2: Schematic of the two transversely quantized azimuthal electron-hole subbands (*left*), and the first-interband ground-internal-state exciton energy (*right*) in a small-diameter semiconducting carbon nanotube. Subbands with indices $j = 1$ and 2 are shown, along with the optically allowed (exciton-related) interband transitions [67]. See text for notations.

only $\sigma_{zz}(R_{CN}, \omega)$, the *axial* dynamic surface conductivity per unit length, is present in Eq.(12).

Equations (1)–(12) form the complete set of equations describing the exciton-photon coupled system on the CN surface in terms of the EM field Green tensor and the CN surface axial conductivity.

3 Exciton-surface-plasmon coupling

For the following it is important to realize that the transversely polarized surface EM mode contribution to the interaction (10)–(12) is negligible compared to the longitudinally polarized surface EM mode contribution. As a matter of fact, ${}^\perp G_{zz}(\mathbf{n}, \mathbf{m}, \omega) \equiv 0$ in the model of an infinitely thin cylinder we use here (Appendix B), thus yielding

$$g_f^\perp(\mathbf{n}, \mathbf{m}, \omega) \equiv 0, \quad g_f^{(\pm)}(\mathbf{n}, \mathbf{m}, \omega) = \pm \frac{\omega}{\omega_f} g_f^\parallel(\mathbf{n}, \mathbf{m}, \omega) \quad (13)$$

in Eqs. (10)–(12). The point is that, because of the nanotube quasi-one-dimensionality, the exciton quasi-momentum vector and all the relevant vectorial matrix elements of the momentum and dipole moment operators are directed predominantly along the CN axis (the longitudinal exciton; see, however, Ref. [70]). This prevents

the exciton from the electric dipole coupling to transversely polarized surface EM modes as they propagate predominantly along the CN axis with their electric vectors orthogonal to the propagation direction. The longitudinally polarized surface EM modes are generated by the electronic Coulomb potential (see, e.g., Ref. [71]), and therefore represent the CN surface plasmon excitations. These have their electric vectors directed along the propagation direction. They do couple to the longitudinal excitons on the CN surface. Such modes were observed in Ref. [50]. They occur in CNs both at high energies (well-known π -plasmon at ~ 6 eV) and at comparatively low energies of $\sim 0.5-2$ eV. The latter ones are related to the transversely quantized interband (inter-van Hove) electronic transitions. These weakly-dispersive modes [50, 72] are similar to the intersubband plasmons in quantum wells [73]. They occur in the same energy range of ~ 1 eV where the exciton excitation energies are located in small-diameter ($\lesssim 1$ nm) semiconducting CNs [51, 52]. In what follows we focus our consideration on the exciton interactions with these particular surface plasmon modes.

3.1 The dispersion relation

To obtain the dispersion relation of the coupled exciton-plasmon excitations, we transfer the total Hamiltonian (1)–(10) and (13) to the \mathbf{k} -representation using Eqs. (5) and (9), and then diagonalize it exactly by means of Bogoliubov's canonical transformation technique (see, e.g., Ref. [74]). The details of the procedure are given in Appendix C. The Hamiltonian takes the form

$$\hat{H} = \sum_{\mathbf{k}, \mu=1,2} \hbar\omega_{\mu}(\mathbf{k}) \hat{\xi}_{\mu}^{\dagger}(\mathbf{k}) \hat{\xi}_{\mu}(\mathbf{k}) + E_0. \quad (14)$$

Here, the new operator

$$\begin{aligned} \hat{\xi}_{\mu}(\mathbf{k}) = & \sum_f \left[u_{\mu}^*(\mathbf{k}, \omega_f) B_{\mathbf{k},f} - v_{\mu}(\mathbf{k}, \omega_f) B_{-\mathbf{k},f}^{\dagger} \right] \\ & + \int_0^{\infty} d\omega \left[u_{\mu}(\mathbf{k}, \omega) \hat{f}(\mathbf{k}, \omega) - v_{\mu}^*(\mathbf{k}, \omega) \hat{f}^{\dagger}(-\mathbf{k}, \omega) \right] \end{aligned} \quad (15)$$

annihilates and $\hat{\xi}_{\mu}^{\dagger}(\mathbf{k}) = [\hat{\xi}_{\mu}(\mathbf{k})]^{\dagger}$ creates the exciton-plasmon excitation of branch μ , the quantities u_{μ} and v_{μ} are appropriately chosen canonical transformation coefficients. The "vacuum" energy E_0 represents the state with no exciton-plasmons excited in the system, and $\hbar\omega_{\mu}(\mathbf{k})$ is the exciton-plasmon energy given by the solution of the following (dimensionless) dispersion relation

$$x_{\mu}^2 - \varepsilon_f^2 - \varepsilon_f \frac{2}{\pi} \int_0^{\infty} dx \frac{x \bar{\Gamma}_0^f(x) \rho(x)}{x_{\mu}^2 - x^2} = 0. \quad (16)$$

Here,

$$x = \frac{\hbar\omega}{2\gamma_0}, \quad x_{\mu} = \frac{\hbar\omega_{\mu}(\mathbf{k})}{2\gamma_0}, \quad \varepsilon_f = \frac{E_f(\mathbf{k})}{2\gamma_0} \quad (17)$$

with $\gamma_0 = 2.7$ eV being the carbon nearest neighbor overlap integral entering the CN surface axial conductivity $\sigma_{zz}(R_{CN}, \omega)$. The function

$$\bar{\Gamma}_0^f(x) = \frac{4|d_z^f|^2 x^3}{3\hbar c^3} \left(\frac{2\gamma_0}{\hbar} \right)^2 \quad (18)$$

with $d_z^f = \sum_{\mathbf{n}} \langle 0 | (\hat{\mathbf{d}}_{\mathbf{n}})_z | f \rangle$ represents the (dimensionless) spontaneous decay rate, and

$$\rho(x) = \frac{3S_0}{16\pi\alpha R_{CN}^2} \operatorname{Re} \frac{1}{\bar{\sigma}_{zz}(x)} \quad (19)$$

stands for the surface plasmon density of states (DOS) which is responsible for the exciton decay rate variation due to its coupling to the plasmon modes. Here, $\alpha = e^2/\hbar c = 1/137$ is the fine-structure constant and $\bar{\sigma}_{zz} = 2\pi\hbar\sigma_{zz}/e^2$ is the dimensionless CN surface axial conductivity per unit length.

Note that the conductivity factor in Eq. (19) equals

$$\operatorname{Re} \frac{1}{\bar{\sigma}_{zz}(x)} = -\frac{4\alpha c}{R_{CN}} \left(\frac{\hbar}{2\gamma_0 x} \right) \operatorname{Im} \frac{1}{\epsilon_{zz}(x) - 1} \quad (20)$$

in view of Eq. (17) and equation

$$\sigma_{zz}(x) = -\frac{i\omega}{4\pi S \rho_T} [\epsilon_{zz}(x) - 1] \quad (21)$$

representing the Drude relation for CNs, where ϵ_{zz} is the longitudinal (along the CN axis) dielectric function, S and ρ_T are the surface area of the tubule and the number of tubules per unit volume, respectively [59, 62, 64]. This relates very closely the surface plasmon DOS function (19) to the loss function $-\operatorname{Im}(1/\epsilon)$ measured in Electron Energy Loss Spectroscopy (EELS) experiments to determine the properties of collective electronic excitations in solids [50].

Figure 3 shows the low-energy behaviors of $\bar{\sigma}_{zz}(x)$ and $\operatorname{Re}[1/\bar{\sigma}_{zz}(x)]$ for the (11,0) and (10,0) CNs ($R_{CN} = 0.43$ nm and 0.39 nm, respectively) we study here. We obtained them numerically as follows. First, we adapt the nearest-neighbor non-orthogonal tight-binding approach [75] to determine the realistic band structure of each CN. Then, the room-temperature longitudinal dielectric functions ϵ_{zz} are calculated within the random-phase approximation [76, 77], which are then converted into the conductivities $\bar{\sigma}_{zz}$ by means of the Drude relation. Electronic dissipation processes are included in our calculations within the relaxation-time approximation (electron scattering length of $130R_{CN}$ was used [30]). We did not include excitonic many-electron correlations, however, as they mostly affect the real conductivity $\operatorname{Re}(\bar{\sigma}_{zz})$ which is responsible for the CN optical absorption [20, 22, 67], whereas we are interested here in $\operatorname{Re}(1/\bar{\sigma}_{zz})$ representing the surface plasmon DOS according to Eq. (19). This function is only non-zero when the two conditions, $\operatorname{Im}[\bar{\sigma}_{zz}(x)] = 0$ and $\operatorname{Re}[\bar{\sigma}_{zz}(x)] \rightarrow 0$, are fulfilled simultaneously [72, 73, 76]. These result in the

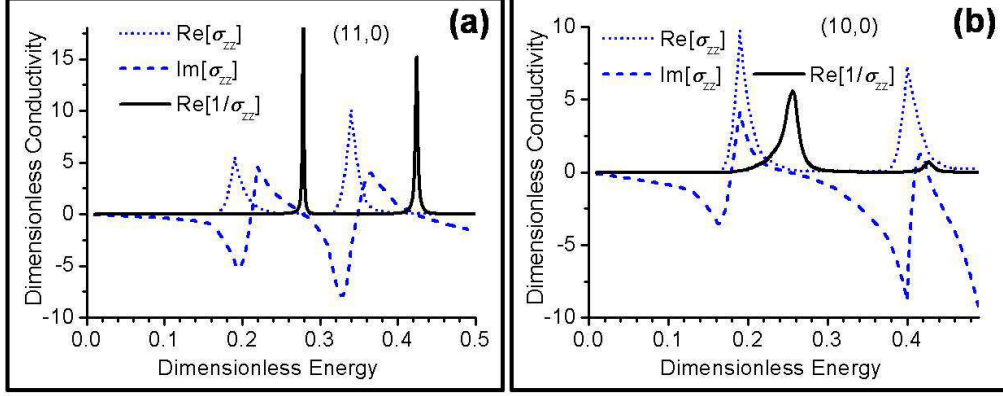


Figure 3: (a),(b) Calculated dimensionless (see text) axial surface conductivities for the (11,0) and (10,0) CNs. The dimensionless energy is defined as $[Energy]/2\gamma_0$, according to Eq. (17).

peak structure of the function $\text{Re}(1/\bar{\sigma}_{zz})$ as is seen in Fig. 3. It is also seen from the comparison of Fig. 3 (b) with Fig. 3 (a) that the peaks broaden as the CN diameter decreases. This is consistent with the stronger hybridization effects in smaller-diameter CNs [78].

Left panels in Figs. 4(a) and 4(b) show the lowest-energy plasmon DOS resonances calculated for the (11,0) and (10,0) CNs as given by the function $\rho(x)$ in Eq. (19). Also shown there are the corresponding fragments of the functions $\text{Re}[\bar{\sigma}_{zz}(x)]$ and $\text{Im}[\bar{\sigma}_{zz}(x)]$. In all graphs the lower dimensionless energy limits are set up to be equal to the lowest bright exciton excitation energy $[E_{exc}^{(11)} = 1.21 \text{ eV}$ ($x = 0.224$) and 1.00 eV ($x = 0.185$) for the (11,0) and (10,0) CN, respectively, as reported in Ref.[51] by directly solving the Bethe-Salpeter equation]. Peaks in $\rho(x)$ are seen to coincide in energy with zeros of $\text{Im}[\bar{\sigma}_{zz}(x)]$ {or zeros of $\text{Re}[\epsilon_{zz}(x)]$ }, clearly indicating the plasmonic nature of the CN surface excitations under consideration [72, 79]. They describe the surface plasmon modes associated with the transversely quantized interband electronic transitions in CNs [72]. As is seen in Fig. 4 (and in Fig. 3), the interband plasmon excitations occur in CNs slightly above the first bright exciton excitation energy [67], in the frequency domain where the imaginary conductivity (or the real dielectric function) changes its sign. This is a unique feature of the complex dielectric response function, the consequence of the general Kramers-Krönig relation [47].

We further take advantage of the sharp peak structure of $\rho(x)$ and solve the dispersion equation (16) for x_μ analytically using the Lorentzian approximation

$$\rho(x) \approx \frac{\rho(x_p)\Delta x_p^2}{(x - x_p)^2 + \Delta x_p^2}. \quad (22)$$

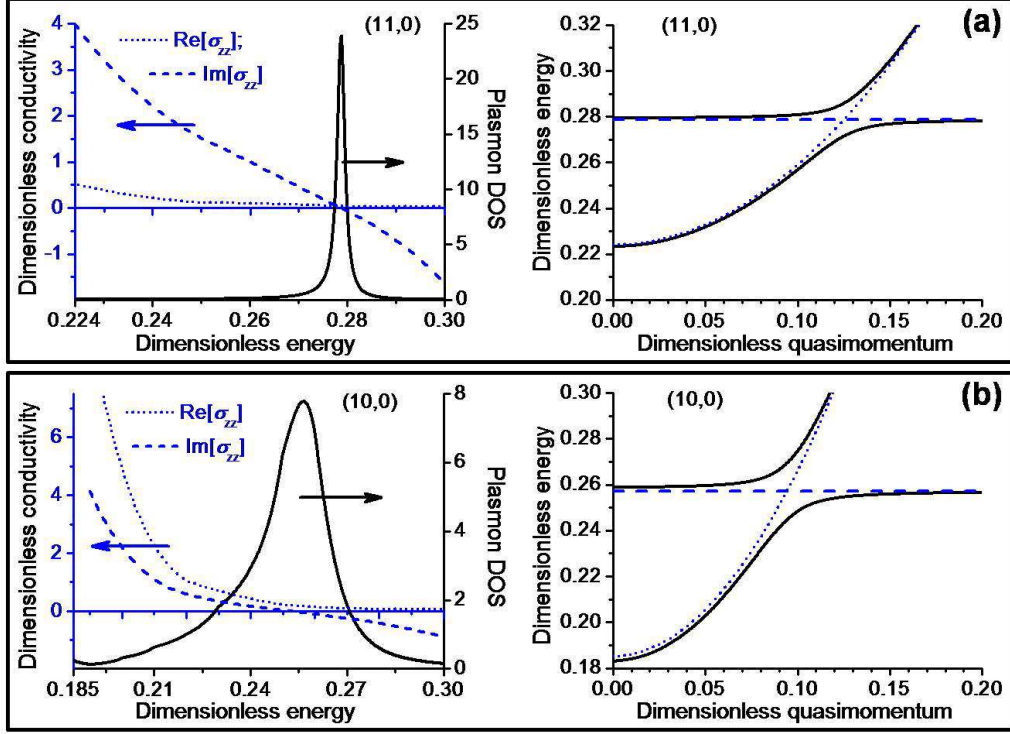


Figure 4: (a),(b) Surface plasmon DOS and conductivities (left panels), and lowest bright exciton dispersion when coupled to plasmons (right panels) in (11,0) and (10,0) CNs, respectively. The dimensionless energy is defined as $[Energy]/2\gamma_0$, according to Eq. (17). See text for the dimensionless quasi-momentum.

Here, x_p and Δx_p are, respectively, the position and the half-width-at-half-maximum of the plasmon resonance closest to the lowest bright exciton excitation energy in the same nanotube (as shown in the left panels of Fig. 4). The integral in Eq. (16) then simplifies to the form

$$\begin{aligned} \frac{2}{\pi} \int_0^\infty dx \frac{x \bar{\Gamma}_0^f(x) \rho(x)}{x_\mu^2 - x^2} &\approx \frac{F(x_p) \Delta x_p^2}{x_\mu^2 - x_p^2} \int_0^\infty \frac{dx}{(x - x_p)^2 + \Delta x_p^2} \\ &= \frac{F(x_p) \Delta x_p}{x_\mu^2 - x_p^2} \left[\arctan\left(\frac{x_p}{\Delta x_p}\right) + \frac{\pi}{2} \right] \end{aligned}$$

with $F(x_p) = 2x_p \bar{\Gamma}_0^f(x_p) \rho(x_p) / \pi$. This expression is valid for all x_μ apart from those located in the narrow interval $(x_p - \Delta x_p, x_p + \Delta x_p)$ in the vicinity of the plasmon resonance, provided that the resonance is sharp enough. Then, the dispersion equation becomes the biquadratic equation for x_μ with the following two positive solutions (the dispersion curves) of interest to us

$$x_{1,2} = \sqrt{\frac{\varepsilon_f^2 + x_p^2}{2}} \pm \frac{1}{2} \sqrt{(\varepsilon_f^2 - x_p^2)^2 + F_p \varepsilon_f}. \quad (23)$$

Here, $F_p = 4F(x_p)\Delta x_p(\pi - \Delta x_p/x_p)$ with the arctan-function expanded to linear terms in $\Delta x_p/x_p \ll 1$.

The dispersion curves (23) are shown in the right panels in Figs. 4(a) and 4(b) as functions of the dimensionless longitudinal quasi-momentum. In these calculations, we estimated the interband transition matrix element in $\bar{\Gamma}_0^f(x_p)$ [Eq.(18)] from the equation $|d_f|^2 = 3\hbar\lambda^3/4\tau_{ex}^{rad}$ according to Hanamura's general theory of the exciton radiative decay in spatially confined systems [80], where τ_{ex}^{rad} is the exciton intrinsic radiative lifetime, and $\lambda = 2\pi c\hbar/E$ with E being the exciton total energy given in our case by Eq. (6). For zigzag-type CNs considered here, the first Brillouin zone of the longitudinal quasi-momentum is given by $-2\pi\hbar/3b \leq \hbar k_z \leq 2\pi\hbar/3b$ [1, 2]. The total energy of the ground-internal-state exciton can then be written as $E = E_{exc} + (2\pi\hbar/3b)^2 t^2 / 2M_{ex}$ with $-1 \leq t \leq 1$ representing the dimensionless longitudinal quasi-momentum. In our calculations we used the lowest bright exciton parameters $E_{exc}^{(11)} = 1.21$ eV and 1.00 eV, $\tau_{ex}^{rad} = 14.3$ ps and 19.1 ps, $M_{ex} = 0.44m_0$ and $0.19m_0$ (m_0 is the free-electron mass) for the (11,0) CN and (10,0) CN, respectively, as reported in Ref.[51] by directly solving the Bethe-Salpeter equation.

Both graphs in the right panels in Fig. 4 are seen to demonstrate a clear anticrossing behavior with the (Rabi) energy splitting ~ 0.1 eV. This indicates the formation of the strongly coupled surface plasmon-exciton excitations in the nanotubes under consideration. It is important to realize that here we deal with the strong exciton-plasmon interaction supported by an individual quasi-1D nanostructure — a single-walled (small-diameter) semiconducting carbon nanotube, as opposed to the artificially fabricated metal-semiconductor nanostructures studied previously [53, 54, 55] where the metallic component normally carries the plasmon and the semiconducting one carries the exciton. It is also important that the effect comes not only from the height but also from the width of the plasmon resonance as it is seen from the definition of the F_p factor in Eq. (23). In other words, as long as the plasmon resonance is sharp enough (which is always the case for interband plasmons), so that the Lorentzian approximation (22) applies, the effect is determined by the area under the plasmon peak in the DOS function (19) rather than by the peak height as one would expect.

However, the formation of the strongly coupled exciton-plasmon states is only possible if the exciton total energy is in resonance with the energy of a surface plasmon mode. The exciton energy can be tuned to the nearest plasmon resonance in ways used for excitons in semiconductor quantum microcavities — thermally [81, 82, 83] (by elevating sample temperature), or/and electrostatically [84, 85, 86, 87] (via the quantum confined Stark effect with an external electrostatic field applied perpendicular to the CN axis). As is seen from Eqs. (6) and (7), the two possibilities influence the different degrees of freedom of the quasi-1D exciton — the (longitudi-

nal) kinetic energy and the excitation energy, respectively. Below we study the (less trivial) electrostatic field effect on the exciton excitation energy in CNs.

3.2 The perpendicular electrostatic field effect

The optical properties of semiconducting CNs in an external electrostatic field directed along the nanotube axis were studied theoretically in Ref. [40]. Strong oscillations in the band-to-band absorption and the quadratic Stark shift of the exciton absorption peaks with the field increase, as well as the strong field dependence of the exciton ionization rate, were predicted for CNs of different diameters and chiralities. Here, we focus on the perpendicular electrostatic field orientation. We study how the electrostatic field applied perpendicular to the CN axis affects the CN band gap, the exciton binding/excitation energy, and the interband surface plasmon energy, to explore the tunability of the strong exciton-plasmon coupling effect predicted above. The problem is similar to the well-known quantum confined Stark effect first observed for the excitons in semiconductor quantum wells [84, 85]. However, the cylindrical surface symmetry of the excitonic states brings new peculiarities to the quantum confined Stark effect in CNs. In what follows we will generally be interested only in the lowest internal energy (ground) excitonic state, and so the internal state index f in Eqs. (6) and (7) will be omitted for brevity.

Because the nanotube is modelled by a continuous, infinitely thin, anisotropically conducting cylinder in our macroscopic QED approach, the actual local symmetry of the excitonic wave function resulted from the graphene Brillouin zone structure is disregarded in our model (see, e.g., reviews [41, 67]). The local symmetry is implicitly present in the surface axial conductivity though, which we calculate beforehand as described above.²

We start with the Schrödinger equation for the electron and hole on the CN surface, located at $\mathbf{r}_e = \{R_{CN}, \varphi_e, z_e\}$ and $\mathbf{r}_h = \{R_{CN}, \varphi_h, z_h\}$, respectively. They interact with each other through the Coulomb potential $V(\mathbf{r}_e, \mathbf{r}_h) = -e^2/\epsilon|\mathbf{r}_e - \mathbf{r}_h|$, where $\epsilon = \epsilon_{zz}(0)$. The external electrostatic field $\mathbf{F} = \{F, 0, 0\}$ is directed perpendicular to the CN axis (along the x -axis in Fig. 1). The Schrödinger equation is of the form

$$\left[\hat{H}_e(\mathbf{F}) + \hat{H}_h(\mathbf{F}) + V(\mathbf{r}_e, \mathbf{r}_h) \right] \Psi(\mathbf{r}_e, \mathbf{r}_h) = E\Psi(\mathbf{r}_e, \mathbf{r}_h) \quad (24)$$

²In real CNs, the existence of two equivalent energy valleys in the 1st Brillouin zone, the K - and K' -valleys with opposite electron helicities about the CN axis, results into dark and bright excitonic states in the lowest energy spin-singlet manifold [88]. Since the electric interaction does not involve spin variables, both K - and K' -valleys are affected equally by the electrostatic field in our case, and the detailed structure of the exciton wave function multiplet is not important. This is opposite to the non-zero magnetostatic field case where the field affects the K - and K' -valleys differently either to brighten the dark excitonic states [39], or to create Landau sublevels [67] for longitudinal and perpendicular orientation, respectively.

with

$$\hat{H}_{e,h}(\mathbf{F}) = -\frac{\hbar^2}{2m_{e,h}} \left(\frac{1}{R_{CN}^2} \frac{\partial^2}{\partial \varphi_{e,h}^2} + \frac{\partial^2}{\partial z_{e,h}^2} \right) \mp e\mathbf{r}_{e,h} \cdot \mathbf{F} \quad (25)$$

We further separate out the translational and relative degrees of freedom of the electron-hole pair by transforming the longitudinal (along the CN axis) motion of the pair into its center-of-mass coordinates given by $Z = (m_e z_e + m_h z_h)/M_{ex}$ and $z = z_e - z_h$. The exciton wave function is approximated as follows

$$\Psi(\mathbf{r}_e, \mathbf{r}_h) = e^{ik_z Z} \phi_{ex}(z) \psi_e(\varphi_e) \psi_h(\varphi_h). \quad (26)$$

The complex exponential describes the exciton center-of-mass motion with the longitudinal quasi-momentum k_z along the CN axis. The function $\phi_{ex}(z)$ represents the longitudinal relative motion of the electron and the hole inside the exciton. The functions $\psi_e(\varphi_e)$ and $\psi_h(\varphi_h)$ are the electron and hole subband wave functions, respectively, which represent their confined motion along the circumference of the cylindrical nanotube surface.

Each of the functions is assumed to be normalized to unity. Equations (24) and (25) are then rewritten in view of Eqs. (6)–(8) to yield

$$\left[-\frac{\hbar^2}{2m_e R_{CN}^2} \frac{\partial^2}{\partial \varphi_e^2} - eR_{CN} F \cos(\varphi_e) \right] \psi_e(\varphi_e) = \varepsilon_e \psi_e(\varphi_e), \quad (27)$$

$$\left[-\frac{\hbar^2}{2m_h R_{CN}^2} \frac{\partial^2}{\partial \varphi_h^2} + eR_{CN} F \cos(\varphi_h) \right] \psi_h(\varphi_h) = \varepsilon_h \psi_h(\varphi_h), \quad (28)$$

$$\left[-\frac{\hbar^2}{2\mu} \frac{\partial^2}{\partial z^2} + V_{\text{eff}}(z) \right] \phi_{ex}(z) = E_b \phi_{ex}(z), \quad (29)$$

where $\mu = m_e m_h / M_{ex}$ is the exciton reduced mass, and V_{eff} is the effective longitudinal electron-hole Coulomb interaction potential given by

$$V_{\text{eff}}(z) = -\frac{e^2}{\epsilon} \int_0^{2\pi} d\varphi_e \int_0^{2\pi} d\varphi_h |\psi_e(\varphi_e)|^2 |\psi_h(\varphi_h)|^2 V(\varphi_e, \varphi_h, z) \quad (30)$$

with V being the original electron-hole Coulomb potential written in the cylindrical coordinates as

$$V(\varphi_e, \varphi_h, z) = \frac{1}{\{z^2 + 4R_{CN}^2 \sin^2[(\varphi_e - \varphi_h)/2]\}^{1/2}}. \quad (31)$$

The exciton problem is now reduced to the 1D equation (29), where the exciton binding energy does depend on the perpendicular electrostatic field through the electron and hole subband functions $\psi_{e,h}$ given by the solutions of Eqs. (27) and (28) and entering the effective electron-hole Coulomb interaction potential (30).

The set of Eqs. (27)-(31) is analyzed in Appendix D. One of the main results obtained in there is that the effective Coulomb potential (30) can be approximated by an attractive cusp-type cutoff potential of the form

$$V_{\text{eff}}(z) \approx -\frac{e^2}{\epsilon[|z| + z_0(j, F)]}, \quad (32)$$

where the cutoff parameter z_0 depends on the perpendicular electrostatic field strength and on the electron-hole azimuthal transverse quantization index $j = 1, 2, \dots$ (excitons are created in interband transitions involving valence and conduction subbands with the same quantization index [67] as shown in Fig. 2). Specifically,

$$z_0(j, F) \approx 2R_{CN} \frac{\pi - 2 \ln 2 [1 - \Delta_j(F)]}{\pi + 2 \ln 2 [1 - \Delta_j(F)]} \quad (33)$$

with $\Delta_j(F)$ given to the second order approximation in the electric field by

$$\begin{aligned} \Delta_j(F) &\approx 2\mu M_{ex} \frac{e^2 R_{CN}^6 w_j^2}{\hbar^4} F^2, \\ w_j &= \frac{\theta(j-2)}{1-2j} + \frac{1}{1+2j}, \end{aligned} \quad (34)$$

where $\theta(x)$ is the unit step function. Approximation (32) is formally valid when $z_0(j, F)$ is much less than the exciton Bohr radius a_B^* ($= \epsilon \hbar^2 / \mu e^2$) which is estimated to be $\sim 10R_{CN}$ for the first ($j=1$ in our notations here) exciton in CNs [19]. As is seen from Eqs. (33) and (34), this is always the case for the first exciton for those fields where the perturbation theory applies, i. e. when $\Delta_1(F) < 1$ in Eq. (34).

Equation (29) with the potential (32) formally coincides with the one studied by Ogawa and Takagahara in their treatments of excitonic effects in 1D semiconductors with no external electrostatic field applied [89]. The only difference in our case is that our cutoff parameter (33) is field dependent. We therefore follow Ref. [89] and find the ground-state binding energy $E_b^{(11)}$ for the first exciton we are interested in here from the transcendental equation

$$\ln \left[\frac{2z_0(1, F)}{\hbar} \sqrt{2\mu |E_b^{(11)}|} \right] + \frac{1}{2} \sqrt{\frac{|E_b^{(11)}|}{Ry^*}} = 0. \quad (35)$$

In doing so, we first find the exciton Rydberg energy, Ry^* ($= \mu e^4 / 2\hbar^2 \epsilon^2$), from this equation at $F=0$. We use the diameter- and chirality-dependent electron and hole effective masses from Ref. [90], and the first bright exciton binding energy of 0.76 eV for both (11,0) and (10,0) CN as reported in Ref. [21] from *ab initio* calculations. We obtain $Ry^* = 4.02$ eV and 0.57 eV for the (11,0) tube and (10,0) tube, respectively. The difference of about one order of magnitude reflects the fact that these are the semiconducting CNs of different types — type-I and type-II, respectively, based on

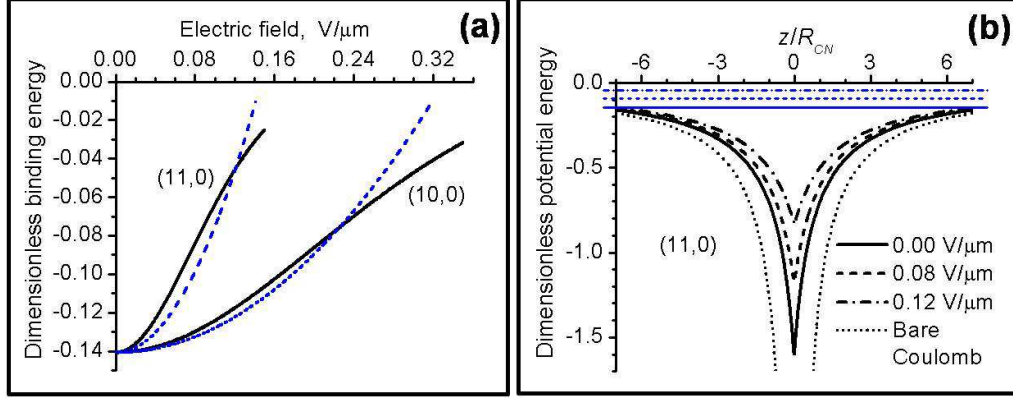


Figure 5: (a) Calculated binding energies of the first bright exciton in the (11,0) and (10,0) CNs as functions of the perpendicular electrostatic field applied. Solid lines are the numerical solutions to Eq. (35), dashed lines are the quadratic approximations as given by Eq. (36). (b) Field dependence of the effective cutoff Coulomb potential (32) in the (11,0) CN. The dimensionless energy is defined as $[Energy]/2\gamma_0$, according to Eq. (17).

$(2n + m)$ families [90]. The parameters Ry^* thus obtained are then used to find $|E_b^{(11)}|$ as functions of F by numerically solving Eq. (35) with $z_0(1, F)$ given by Eqs. (33) and (34).

The calculated (negative) binding energies are shown in Fig. 5(a) by the solid lines. Also shown there by dashed lines are the functions

$$E_b^{(11)}(F) \approx E_b^{(11)}[1 - \Delta_1(F)] \quad (36)$$

with $\Delta_1(F)$ given by Eq. (34). They are seen to be fairly good analytical (quadratic in field) approximations to the numerical solutions of Eq. (35) in the range of not too large fields. The exciton binding energy decreases very rapidly in its absolute value as the field increases. Fields of only $\sim 0.1 - 0.2$ V/μm are required to decrease $|E_b^{(11)}|$ by a factor of ~ 2 for the CNs considered here. The reason is the perpendicular field shifts up the "bottom" of the effective potential (32) as shown in Fig. 5(b) for the (11,0) CN. This makes the potential shallower and pushes bound excitonic levels up, thereby decreasing the exciton binding energy in its absolute value. As this takes place, the shape of the potential does not change, and the longitudinal relative electron-hole motion remains finite at all times. As a consequence, no tunnel exciton ionization occurs in the perpendicular field, as opposed to the longitudinal electrostatic field (Franz-Keldysh) effect studied in Ref. [40] where the non-zero field creates the potential barrier separating out the regions of finite and infinite relative motion and the exciton becomes ionized as the electron tunnels to infinity.

The binding energy is only the part of the exciton excitation energy (7). Another

part comes from the band gap energy (8), where ε_e and ε_h are given by the solutions of Eqs. (27) and (28), respectively. Solving them to the leading (second) order perturbation theory approximation in the field (Appendix D), one obtains

$$E_g^{(jj)}(F) \approx E_g^{(jj)} \left[1 - \frac{m_e \Delta_j(F)}{2M_{ex} j^2 w_j} - \frac{m_h \Delta_j(F)}{2M_{ex} j^2 w_j} \right], \quad (37)$$

where the electron and hole subband shifts are written separately. This, in view of Eq. (34), yields the first band gap field dependence in the form

$$E_g^{(11)}(F) \approx E_g^{(11)} \left[1 - \frac{3}{2} \Delta_1(F) \right], \quad (38)$$

The band gap decrease with the field in Eq. (38) is stronger than the opposite effect in the negative exciton binding energy given (to the same order approximation in field) by Eq. (36). Thus, the first exciton excitation energy (7) will be gradually decreasing as the perpendicular field increases, shifting the exciton absorption peak to the red. This is the basic feature of the quantum confined Stark effect observed previously in semiconductor nanomaterials [84, 85, 86, 87]. The field dependences of the higher interband transitions exciton excitation energies are suppressed by the rapidly (quadratically) increasing azimuthal quantization numbers in the denominators of Eqs. (34) and (37).

Lastly, the perpendicular field dependence of the interband plasmon resonances can be obtained from the frequency dependence of the axial surface conductivity due to excitons (see Ref. [67] and refs. therein). One has

$$\sigma_{zz}^{ex}(\omega) \sim \sum_{j=1,2,\dots} \frac{-i\hbar\omega f_j}{[E_{exc}^{(jj)}]^2 - (\hbar\omega)^2 - 2i\hbar^2\omega/\tau}, \quad (39)$$

where f_j and τ are the exciton oscillator strength and relaxation time, respectively. The plasmon frequencies are those at which the function $\text{Re}[1/\sigma_{zz}^{ex}(\omega)]$ has maxima. Testing it for maximum in the domain $E_{exc}^{(11)} < \hbar\omega < E_{exc}^{(22)}$, one finds the first interband plasmon resonance energy to be (in the limit $\tau \rightarrow \infty$)

$$E_p^{(11)} = \sqrt{\frac{[E_{exc}^{(11)}]^2 + [E_{exc}^{(22)}]^2}{2}}. \quad (40)$$

Using the field dependent $E_{exc}^{(11)}$ given by Eqs. (7), (36) and (38), and neglecting the field dependence of $E_{exc}^{(22)}$, one obtains to the second order approximation in the field

$$E_p^{(11)}(F) \approx E_p^{(11)} \left[1 - \frac{1 + E_g^{(11)}/2E_{exc}^{(11)}}{1 + E_{exc}^{(22)}/E_{exc}^{(11)}} \Delta_1(F) \right]. \quad (41)$$

Figure 6 shows the results of our calculations of the field dependences for the first bright exciton parameters in the (11,0) and (10,0) CNs. The energy is measured

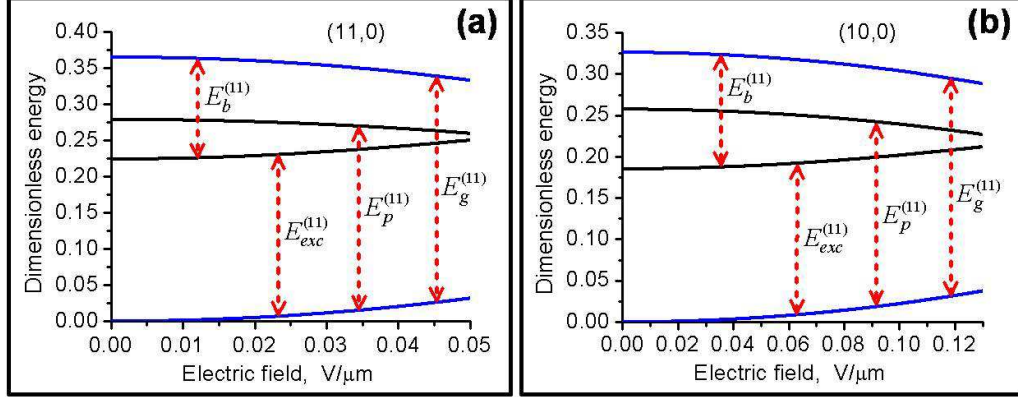


Figure 6: (a),(b) Calculated dependences of the first bright exciton parameters in the (11,0) and (10,0) CNs, respectively, on the electrostatic field applied perpendicular to the nanotube axis. The dimensionless energy is defined as $[Energy]/2\gamma_0$, according to Eq. (17). The energy is measured from the top of the first unperturbed hole subband.

from the top of the first unperturbed hole subband (as shown in Fig. 2, right panel). The binding energy field dependence was calculated numerically from Eq. (35) as described above [shown in Fig. 5 (a)]. The band gap field dependence and the plasmon energy field dependence were calculated from Eqs. (37) and (41), respectively. The zero-field excitation energies and zero-field binding energies were taken to be those reported in Ref. [51] and in Ref. [21], respectively, and we used the diameter- and chirality-dependent electron and hole effective masses from Ref. [90]. As is seen in Fig. 6 (a) and (b), the exciton excitation energy and the interband plasmon energy experience red shift in both nanotubes as the field increases. However, the excitation energy red shift is very small (barely seen in the figures) due to the negative field dependent contribution from the exciton binding energy. So, $E_{exc}^{(11)}(F)$ and $E_p^{(11)}(F)$ approach each other as the field increases, thereby bringing the total exciton energy (6) in resonance with the surface plasmon mode due to the non-zero longitudinal kinetic energy term at finite temperature.³ Thus, the electrostatic field applied perpendicular to the CN axis (the quantum confined Stark effect) may be used to tune the exciton energy to the nearest interband plasmon resonance, to put the exciton-surface plasmon interaction in small-diameter semiconducting CNs to the strong-coupling regime.

³We are based on the zero-exciton-temperature approximation in here [91], which is well justified because of the exciton excitation energies much larger than $k_B T$ in CNs. The exciton Hamiltonian (4) does not require the thermal averaging over the exciton degrees of freedom then, yielding the temperature independent total exciton energy (6). One has to keep in mind, however, that the exciton excitation energy can be affected by the environmental effect not under consideration in here (see Ref. [92]).

3.3 The optical absorption

Here, we analyze the longitudinal exciton absorption line shape as its energy is tuned to the nearest interband surface plasmon resonance. Only longitudinal excitons (excited by light polarized along the CN axis) couple to the surface plasmon modes as discussed at the very beginning of this section (see Ref. [70] for the perpendicular light exciton absorption in CNs). We start with the linear (weak) excitation regime where only single-exciton states are excited, and follow the optical absorption/emission lineshape theory developed recently for atomically doped CNs [10]. (Obviously, the absorption line shape coincides with the emission line shape if the monochromatic incident light beam is used in the absorption experiment.) Then, the non-linear (strong) excitation regime is considered with the photogenerated excitation of biexciton states.

When the f -internal state exciton is excited and the nanotube's surface EM field subsystem is in vacuum state, the time-dependent wave function of the whole system "exciton+field" is of the form⁴

$$|\psi(t)\rangle = \sum_{\mathbf{k},f} C_f(\mathbf{k},t) e^{-i\tilde{E}_f(\mathbf{k})t/\hbar} |\{1_f(\mathbf{k})\}\rangle_{ex} |\{0\}\rangle \quad (42)$$

$$+ \sum_{\mathbf{k}} \int_0^\infty d\omega C(\mathbf{k},\omega,t) e^{-i\omega t} |\{0\}\rangle_{ex} |\{1(\mathbf{k},\omega)\}\rangle.$$

Here, $|\{1_f(\mathbf{k})\}\rangle_{ex}$ is the excited single-quantum Fock state with one exciton and $|\{1(\mathbf{k},\omega)\}\rangle$ is that with one surface photon. The vacuum states are $|\{0\}\rangle_{ex}$ and $|\{0\}\rangle$ for the exciton subsystem and field subsystem, respectively. The coefficients $C_f(\mathbf{k},t)$ and $C(\mathbf{k},\omega,t)$ stand for the population probability amplitudes of the respective states of the whole system. The exciton energy is of the form $\tilde{E}_f(\mathbf{k}) = E_f(\mathbf{k}) - i\hbar/\tau$ with $E_f(\mathbf{k})$ given by Eq. (6) and τ being the phenomenological exciton relaxation time constant [assumed to be such that $\hbar/\tau \ll E_f(\mathbf{k})$] to account for other possible exciton relaxation processes. From the literature we have $\tau_{ph} \sim 30 - 100$ fs for the exciton-phonon scattering [40], $\tau_d \sim 50$ ps for the exciton scattering by defects [25, 28], and $\tau_{rad} \sim 10$ ps – 10 ns for the radiative decay of excitons [51]. Thus, the scattering by phonons is the most likely exciton relaxation mechanism.

Using Eqs.(5) and (9), we transform the total Hamiltonian (1)–(10) to the \mathbf{k} -representation (see Appendix A), and apply it to the wave function in Eq. (42). We obtain the following set of the two simultaneous differential equations for the coefficients $C_f(\mathbf{k},t)$ and $C(\mathbf{k},\omega,t)$ from the time dependent Schrödinger equation

$$\dot{C}_f(\mathbf{k},t) e^{-i\tilde{E}_f(\mathbf{k})t/\hbar} = -\frac{i}{\hbar} \sum_{\mathbf{k}'} \int_0^\infty d\omega g_f^{(+)}(\mathbf{k},\mathbf{k}',\omega) C(\mathbf{k}',\omega,t) e^{-i\omega t}, \quad (43)$$

$$\dot{C}(\mathbf{k}',\omega,t) e^{-i\omega t} \delta_{\mathbf{k}\mathbf{k}'} = -\frac{i}{\hbar} \sum_f [g_f^{(+)}(\mathbf{k},\mathbf{k}',\omega)]^* C_f(\mathbf{k},t) e^{-i\tilde{E}_f(\mathbf{k})t/\hbar}.$$

⁴See the footnote on page 12 above.

The δ -symbol on the left in Eq. (44) ensures that the momentum conservation is fulfilled in the exciton-photon transitions, so that the annihilating exciton creates the surface photon with the same momentum and vice versa. In terms of the probability amplitudes above, the exciton emission intensity distribution is given by the final state probability at very long times corresponding to the complete decay of all initially excited excitons,

$$I(\omega) = |C(\mathbf{k}, \omega, t \rightarrow \infty)|^2 = \frac{1}{\hbar^2} \sum_f |g_f^{(+)}(\mathbf{k}, \mathbf{k}, \omega)|^2 \times \left| \int_0^\infty dt' C_f(\mathbf{k}, t') e^{-i[\tilde{E}_f(\mathbf{k}) - \hbar\omega]t'/\hbar} \right|^2. \quad (44)$$

Here, the second equation is obtained by the formal integration of Eq. (44) over time under the initial condition $C(\mathbf{k}, \omega, 0) = 0$. The emission intensity distribution is thus related to the exciton population probability amplitude $C_f(\mathbf{k}, t)$ to be found from Eq. (43).

The set of simultaneous equations (43) and (44) [and Eq. (44), respectively] contains no approximations except the (commonly used) neglect of many-particle excitations in the wave function (42). We now apply these equations to the exciton-surface-plasmon system in small-diameter semiconducting CNs. The interaction matrix element in Eqs. (43) and (44) is then given by the \mathbf{k} -transform of Eq. (13), and has the following property (Appendix C)

$$\frac{1}{2\gamma_0\hbar} |g_f^{(+)}(\mathbf{k}, \mathbf{k}, \omega)|^2 = \frac{1}{2\pi} \bar{\Gamma}_0^f(x) \rho(x) \quad (45)$$

with $\bar{\Gamma}_0^f(x)$ and $\rho(x)$ given by Eqs. (18) and (19), respectively. We further substitute the result of the formal integration of Eq. (44) [with $C(\mathbf{k}, \omega, 0) = 0$] into Eq. (43), use Eq. (45) with $\rho(x)$ approximated by the Lorentzian (22), calculate the integral over frequency analytically, and differentiate the result over time to obtain the following second order ordinary differential equation for the exciton probability amplitude [dimensionless variables, Eq. (17)]

$$\ddot{C}_f(\beta) + [\Delta x_p - \Delta \varepsilon_f + i(x_p - \varepsilon_f)] \dot{C}_f(\beta) + (X_f/2)^2 C_f(\beta) = 0,$$

where $X_f = [2\Delta x_p \bar{\Gamma}_f(x_p)]^{1/2}$ with $\bar{\Gamma}_f(x_p) = \bar{\Gamma}_0^f(x_p) \rho(x_p)$, $\Delta \varepsilon_f = \hbar/2\gamma_0\tau$, $\beta = 2\gamma_0 t/\hbar$ is the dimensionless time, and the \mathbf{k} -dependence is omitted for brevity. When the total exciton energy is close to a plasmon resonance, $\varepsilon_f \approx x_p$, the solution of this equation is easily found to be

$$C_f(\beta) \approx \frac{1}{2} \left(1 + \frac{\delta x}{\sqrt{\delta x^2 - X_f^2}} \right) e^{-(\delta x - \sqrt{\delta x^2 - X_f^2})\beta/2} + \frac{1}{2} \left(1 - \frac{\delta x}{\sqrt{\delta x^2 - X_f^2}} \right) e^{-(\delta x + \sqrt{\delta x^2 - X_f^2})\beta/2}, \quad (46)$$

where $\delta x = \Delta x_p - \Delta \varepsilon_f > 0$ and $X_f = [2\Delta x_p \bar{\Gamma}_f(\varepsilon_f)]^{1/2}$. This solution is valid when $\varepsilon_f \approx x_p$ regardless of the strength of the exciton-surface-plasmon coupling. It yields the exponential decay of the excitons into plasmons, $|C_f(\beta)|^2 \approx \exp[-\bar{\Gamma}_f(\varepsilon_f)\beta]$, in the weak coupling regime where the coupling parameter $(X_f/\delta x)^2 \ll 1$. If, on the other hand, $(X_f/\delta x)^2 \gg 1$, then the strong coupling regime occurs, and the decay of the excitons into plasmons proceeds via damped Rabi oscillations, $|C_f(\beta)|^2 \approx \exp(-\delta x \beta) \cos^2(X_f \beta/2)$. This is very similar to what was earlier reported for an excited two-level atom near the nanotube surface [58, 59, 60, 9]. Note, however, that here we have the exciton-phonon scattering as well, which facilitates the strong exciton-plasmon coupling by decreasing δx in the coupling parameter. In other words, the phonon scattering broadens the (longitudinal) exciton momentum distribution [93], thus effectively increasing the fraction of the excitons with $\varepsilon_f \approx x_p$.

In view of Eqs. (45) and (46), the exciton emission intensity (44) in the vicinity of the plasmon resonance takes the following (dimensionless) form

$$\bar{I}(x) \approx \bar{I}_0(\varepsilon_f) \sum_f \left| \int_0^\infty d\beta C_f(\beta) e^{i(x-\varepsilon_f+i\Delta\varepsilon_f)\beta} \right|^2, \quad (47)$$

where $\bar{I}(x) = 2\gamma_0 I(\omega)/\hbar$ and $\bar{I}_0 = \bar{\Gamma}_f(\varepsilon_f)/2\pi$. After some algebra, this results in

$$\bar{I}(x) \approx \frac{\bar{I}_0(\varepsilon_f) [(x - \varepsilon_f)^2 + \Delta x_p^2]}{[(x - \varepsilon_f)^2 - X_f^2/4]^2 + (x - \varepsilon_f)^2 (\Delta x_p^2 + \Delta \varepsilon_f^2)}, \quad (48)$$

where $\Delta x_p^2 > \Delta \varepsilon_f^2$. The summation sign over the exciton internal states is omitted since only one internal state contributes to the emission intensity in the vicinity of the sharp plasmon resonance.

The line shape in Eq. (48) is mainly determined by the coupling parameter $(X_f/\Delta x_p)^2$. It is clearly seen to be of a symmetric two-peak structure in the strong coupling regime where $(X_f/\Delta x_p)^2 \gg 1$. Testing it for extremum, we obtain the peak frequencies to be

$$x_{1,2} = \varepsilon_f \pm \frac{X_f}{2} \sqrt{\sqrt{1 + 8 \left(\frac{\Delta x_p}{X_f}\right)^2} - 4 \left(\frac{\Delta x_p}{X_f}\right)^2}$$

[terms $\sim (\Delta x_p)^2 (\Delta \varepsilon_f)^2 / X_f^4$ are neglected], with the Rabi splitting $x_1 - x_2 \approx X_f$. In the weak coupling regime where $(X_f/\Delta x_p)^2 \ll 1$, the frequencies x_1 and x_2 become complex, indicating that there are no longer peaks at these frequencies. As this takes place, Eq. (48) is approximated with the weak coupling condition, the fact that $x \sim \varepsilon_f$, and $X_f^2 = 2\Delta x_p \bar{\Gamma}_f(\varepsilon_f)$, to yield the Lorentzian

$$\tilde{I}(x) \approx \frac{\bar{I}_0(\varepsilon_f)/[1 + (\Delta \varepsilon_f/\Delta x_p)^2]}{(x - \varepsilon_f)^2 + \left[\bar{\Gamma}_f(\varepsilon_f)/2\sqrt{1 + (\Delta \varepsilon_f/\Delta x_p)^2} \right]^2}$$

peaked at $x = \varepsilon_f$, whose half-width-at-half-maximum is slightly narrower, however, than $\bar{\Gamma}_f(\varepsilon_f)/2$ it should be if the exciton-plasmon relaxation were the only relaxation mechanism in the system. The reason is the competing phonon scattering takes excitons out of resonance with plasmons, thus decreasing the exciton-plasmon relaxation rate. We therefore conclude that the phonon scattering does not affect the exciton emission/absorption line shape when the exciton-plasmon coupling is strong (it facilitates the strong coupling regime to occur, however, as was noticed above), and it narrows the (Lorentzian) emission/absorption line when the exciton-plasmon coupling is weak.

The non-linear optical susceptibility is proportional to the linear optical response function under resonant pumping conditions [94]. This allows us to use Eq. (48) to investigate the non-linear excitation regime with the photoinduced biexciton formation as the exciton energy is tuned to the nearest interband plasmon resonance. Under these conditions, the third-order longitudinal CN susceptibility takes the form [32, 94]

$$\chi^{(3)}(x) \approx \tilde{I}(x) \left[\frac{1}{x - \varepsilon_f + i(\Gamma^f/2 + \Delta\varepsilon_f)} - \frac{1}{x - (\varepsilon_f - |\varepsilon_f^{XX}|) + i(\Gamma^f/2 + \Delta\varepsilon_f)} \right], \quad (49)$$

where ε_f^{XX} is the (negative) dimensionless binding energy of the biexciton composed of two f -internal state excitons, and χ_0 is the frequency-independent constant. The first and second terms in the brackets represent bleaching due to the depopulation of the ground state and photoinduced absorption due to exciton-to-biexciton transitions, respectively.

The binding energy of the biexciton in a small-diameter (~ 1 nm) CN can be evaluated by the method pioneered by Landau [95], Gor'kov and Pitaevski [96], Holstein and Herring [97] — from the analysis of the asymptotic exchange coupling by perturbation on the configuration space wave function of the two ground-state one-dimensional (1D) excitons. Separating out circumferential and longitudinal degrees of freedom of each of the excitons by means of Eq. (26), one arrives at the biexciton Hamiltonian of the form [see Fig. 7 (a)]

$$\begin{aligned} \hat{H}(z_1, z_2, \Delta Z) = & -\frac{1}{2} \left(\frac{\partial^2}{\partial z_1^2} + \frac{\partial^2}{\partial z_2^2} \right) \\ & - \frac{1}{2} \left[\frac{1}{|z_1| + z_0} + \frac{1}{|z_2 + \Delta Z| + z_0} + \frac{1}{|z_2| + z_0} + \frac{1}{|z_1 - \Delta Z| + z_0} \right] \\ & - \frac{1}{|(z_1 + z_2)/2 + \Delta Z| + z_0} - \frac{1}{|(z_1 + z_2)/2 - \Delta Z| + z_0} \\ & + \frac{1}{|(z_1 - z_2)/2 + \Delta Z| + z_0} + \frac{1}{|(z_1 - z_2)/2 - \Delta Z| + z_0}. \end{aligned} \quad (50)$$

Here, $z_{1,2} = z_{e1,2} - z_{h1,2}$ is the electron-hole relative motion coordinates of the two 1D excitons, z_0 is the cut-off parameter of the effective longitudinal electron-hole

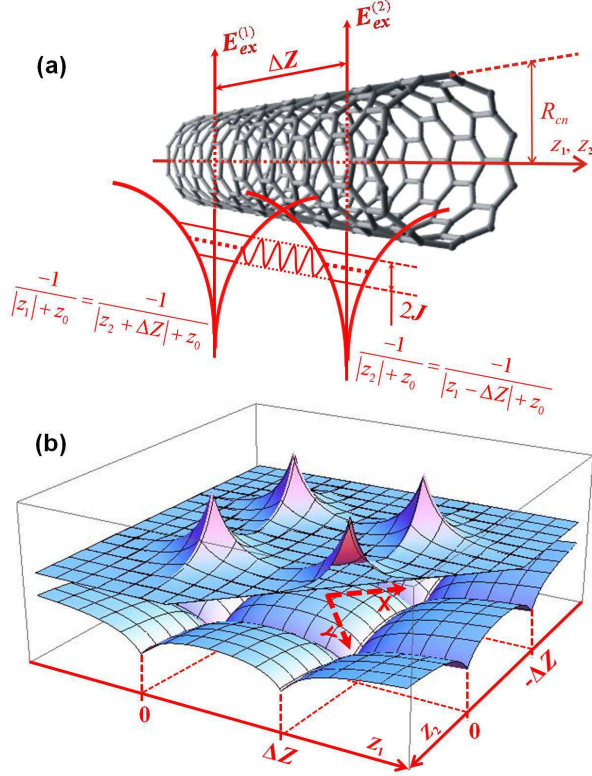


Figure 7: (a) Schematic (arbitrary units) of the exchange coupling of two ground-state 1D excitons to form a biexcitonic state. (b) The coupling occurs in the configuration space of the two independent longitudinal relative electron-hole motion coordinates, z_1 and z_2 , of each of the excitons, due to the tunneling of the system through the potential barriers formed by the two single-exciton cusp-type potentials [bottom, also in (a)], between equivalent states represented by the isolated two-exciton wave functions shown on the top.

Coulomb potential (32), and $\Delta Z = Z_2 - Z_1$ is the center-of-mass-to-center-of-mass inter-exciton separation distance. Equal electron and hole effective masses $m_{e,h}$ are assumed [90] and "atomic units" are used [95, 96, 97], whereby distance and energy are measured in units of the exciton Bohr radius a_B^* and in units of the doubled ground-state-exciton binding energy $2E_b = -2Ry^*/\nu_0^2$, respectively. The first two lines in Eq. (50) represent two isolated non-interacting 1D excitons [see Fig. 7 (a)]. The last two lines are their exchange Coulomb interactions — electron-hole and electron-electron + hole-hole, respectively.

The Hamiltonian (50) is effectively two dimensional in the configuration space of the two *independent* relative motion coordinates, z_1 and z_2 . Figure 7 (b), bottom, shows schematically the potential energy surface of the two closely spaced non-

interacting 1D excitons [line two in Eq. (50)] in the (z_1, z_2) space. The surface has four symmetrical minima [representing *equivalent* isolated two-exciton states shown in Fig. 7 (b), top], separated by the potential barriers responsible for the tunnel exchange coupling between the two-exciton states in the configuration space. The coordinate transformation $x = (z_1 - z_2 - \Delta Z)/\sqrt{2}$, $y = (z_1 + z_2)/\sqrt{2}$ places the origin of the new coordinate system into the intersection of the two tunnel channels between the respective potential minima [Fig. 7 (b)], whereby the exchange splitting formula of Refs. [95, 96, 97] takes the form

$$U_{g,u}(\Delta Z) - 2E_b = \mp J(\Delta Z), \quad (51)$$

where $U_{g,u}$ are the ground and excited state energies, respectively, of the two *coupled* excitons (the biexciton) as functions of their center-of-mass-to-center-of-mass separation, and

$$J(\Delta Z) = \frac{2}{3!} \int_{-\Delta Z/\sqrt{2}}^{\Delta Z/\sqrt{2}} dy \left[\psi(x, y) \frac{\partial \psi(x, y)}{\partial x} \right]_{x=0} \quad (52)$$

is the tunnel exchange coupling integral, where $\psi(x, y)$ is the solution to the Schrödinger equation with the Hamiltonian (50) transformed to the (x, y) coordinates. The factor $2/3!$ comes from the fact that there are two equivalent tunnel channels in the problem, mixing three equivalent indistinguishable two-exciton states in the configuration space [one state is given by the two minima on the y -axis, and two more are represented by each of the minima on the x -axis — compare Figs. 7 (a) and (b)].

The function $\psi(x, y)$ in Eq. (52) is sought in the form

$$\psi(x, y) = \psi_0(x, y) \exp[-S(x, y)], \quad (53)$$

where $\psi_0 = \nu_0^{-1} \exp[-(|z_1(x, y, \Delta Z)| + |z_2(x, y, \Delta Z)|)/\nu_0]$ is the product of two single-exciton wave functions⁵ representing the isolated two-exciton state centered at the minimum $z_1 = z_2 = 0$ (or $x = -\Delta Z/\sqrt{2}$, $y = 0$) of the configuration space potential [Fig. 7 (b)], and $S(x, y)$ is a slowly varying function to take into account the deviation of ψ from ψ_0 due to the tunnel exchange coupling to another equivalent isolated two-exciton state centered at $z_1 = \Delta Z$, $z_2 = -\Delta Z$ (or $x = \Delta Z/\sqrt{2}$, $y = 0$). Substituting Eq. (53) into the Schrödinger equation with the Hamiltonian (50) pre-transformed to the (x, y) coordinates, one obtains in the region of interest

$$\frac{\partial S}{\partial x} = \nu_0 \left(\frac{1}{x + 3\Delta Z/\sqrt{2}} - \frac{1}{x - \Delta Z/\sqrt{2}} + \frac{1}{y - \sqrt{2}\Delta Z} - \frac{1}{y + \sqrt{2}\Delta Z} \right),$$

⁵This is an approximate solution to the Schrödinger equation with the Hamiltonian given by the first two lines in Eq. (50), where the cut-off parameter z_0 is neglected [89]. This approximation greatly simplifies problem solving here, while still remaining adequate as only the long-distance tail of ψ_0 is important for the tunnel exchange coupling.

up to (negligible) terms of the order of the inter-exciton van der Waals energy and up to second derivatives of S . This equation is to be solved with the boundary condition $S(-\Delta Z/\sqrt{2}, y) = 0$ originating from the natural requirement $\psi(-\Delta Z/\sqrt{2}, y) = \psi_0(-\Delta Z/\sqrt{2}, y)$, to result in

$$S(x, y) = \nu_0 \left(\ln \left| \frac{x + 3\Delta Z/\sqrt{2}}{x - \Delta Z/\sqrt{2}} \right| + \frac{2\sqrt{2}\Delta Z(x + \Delta Z/\sqrt{2})}{y^2 - 2\Delta Z^2} \right). \quad (54)$$

After plugging Eqs. (54) and (53) into Eq. (52), and retaining only the leading term of the integral series expansion in powers of ν_0 subject to $\Delta Z > 1$, Eq. (51) becomes

$$U_{g,u}(\Delta Z) \approx 2E_b \left[1 \pm \frac{2}{3\nu_0^2} \left(\frac{e}{3} \right)^{2\nu_0} \Delta Z e^{-2\Delta Z/\nu_0} \right]. \quad (55)$$

The ground state energy U_g of two coupled 1D excitons is now seen to go through the negative minimum (biexcitonic state) as the inter-exciton center-of-mass-to-center-of-mass separation ΔZ increases (Fig. 8). The minimum occurs at $\Delta Z_0 = \nu_0/2$, whereby the biexciton binding energy is $E_{XX} \approx (2E_b/9\nu_0)(e/3)^{2\nu_0-1}$, or, expressing ν_0 in terms of E_b and measuring the energy in units of Ry^* ,

$$E_{XX}[\text{in } Ry^*] \approx -\frac{2}{9} |E_b|^{3/2} \left(\frac{e}{3} \right)^{2/\sqrt{|E_b|}-1}. \quad (56)$$

The energy E_{XX} can be affected by the quantum confined Stark effect since $|E_b|$ decreases quadratically with the perpendicular electrostatic field applied as shown in Fig. 5 (a). Since $e/3 \sim 1$, the field dependence in Eq. (56) mainly comes from the pre-exponential factor. So, $|E_{XX}|$ will be decreasing quadratically with the field as well, for not too strong perpendicular fields. At the same time, the equilibrium inter-exciton separation in the biexciton, $\Delta Z_0 = \nu_0/2 \sim |E_b|^{-1/2}$, will be slowly increasing with the field consistently with the lowering of $|E_{XX}|$. In the zero field, one has roughly $E_{XX} \sim |E_b|^{3/2} \sim R_{CN}^{-0.9}$ for the biexciton binding energy versus the CN radius R_{CN} ($|E_b| \sim R_{CN}^{-0.6}$ as reported in Ref. [19] from variational calculations), pretty consistent with the R_{CN}^{-1} dependence obtained numerically [32]. Interestingly, as R_{CN} goes down, $|E_{XX}|$ goes up faster than $|E_b|$ does. This is partly due to the fact that ΔZ_0 slowly decreases as R_{CN} goes down, — a theoretical argument in support of experimental evidence for increased exciton-exciton annihilation in small diameter CNs [98, 99, 100].

Figure 8 shows the ground state energy $U_g(\Delta Z)$ of the coupled pair of the first bright excitons, calculated from Eq. (55) for the semiconducting (11,0) CN exposed to different perpendicular electrostatic fields. The inset shows the field dependences of E_{XX} [as given by Eq. (56)] and of ΔZ_0 . All the curves are calculated using the field dependence of E_b obtained as described in the previous subsection (Figs. 5 and 6). They exhibit typical behaviors discussed above.

Figure 9 compares the linear response lineshape (48) with the imaginary part of Eq. (49) representing the non-linear optical response function under resonant

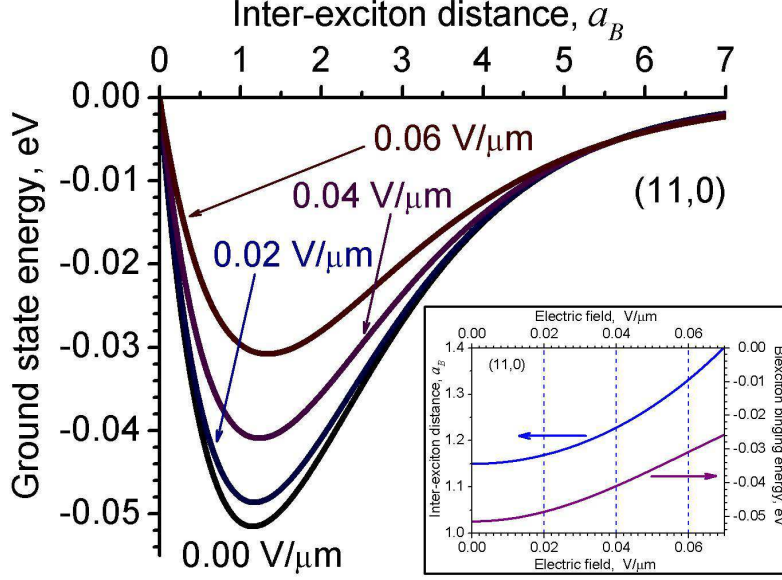


Figure 8: Calculated ground state energy U_g of the coupled pair of the first bright excitons in the (11,0) CN as a function of the center-of-mass-to-center-of-mass inter-exciton distance ΔZ and perpendicular electrostatic field applied. Inset shows the biexciton binding energy E_{XX} and inter-exciton separation ΔZ_0 (y - and x -coordinates, respectively, of the minima in the main figure) as functions of the field.

pumping, both calculated for the 1st bright exciton in the (11,0) CN as its energy is tuned (by means of the quantum confined Stark effect) to the nearest plasmon resonance (vertical dashed line in the figure). The biexciton binding energy in Eq. (49) was taken to be $E_{XX} \approx 52$ meV as given by Eq. (56) in the zero field. [Weak field dependence of E_{XX} (inset in Fig. 8) plays no essential role here as $|E_{XX}| \ll |E_b| \approx 0.76$ eV regardless of the field strength.] The phonon relaxation time $\tau_{ph} = 30$ fs was used as reported in Ref. [29], since this is the shortest one out of possible exciton relaxation processes, including exciton-exciton annihilation ($\tau_{ee} \sim 1$ ps [98]). Clear line (Rabi) splitting effect ~ 0.1 eV is seen both in the linear and in non-linear excitation regime, indicating the strong exciton-plasmon coupling both in the single-exciton states and in the biexciton states as the exciton energy is tuned to the interband surface plasmon resonance. The splitting is not masked by the exciton-phonon scattering.

This effect can be used for the development of new tunable optoelectronic device applications of optically excited small-diameter semiconducting CNs in areas such as nanophotonics, nanoplasmonics, and cavity quantum electrodynamics, including the strong excitation regime with optical non-linearities. In the latter case,

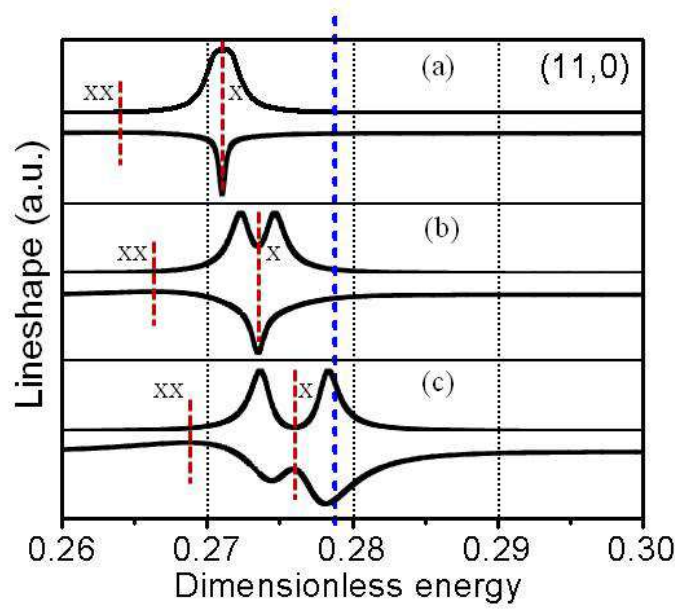


Figure 9: [(a), (b), and (c)] Linear (top) and non-linear (bottom) response functions as given by Eq. (48) and by the imaginary part of Eq. (49), respectively, for the first bright exciton in the (11,0) CN as the exciton energy is tuned to the nearest interband plasmon resonance (vertical dashed line). Vertical lines marked as X and XX show the exciton energy and biexciton binding energy, respectively. The dimensionless energy is defined as $[Energy]/2\gamma_0$, according to Eq. (17).

the experimental observation of the non-linear absorption line splitting predicted here would help identify the presence and study the properties of biexcitonic states (including biexcitons formed by excitons of different subbands [33]) in individual single-walled CNs, due to the fact that when tuned close to a plasmon resonance the exciton relaxes into plasmons at a rate much greater than τ_{ph}^{-1} ($\gg \tau_{ee}^{-1}$), totally ruling out the role of the competing exciton-exciton annihilation process.

4 Casimir Interaction in Double-Wall Carbon Nanotubes

Here, we consider the Casimir interaction between two concentric cylindrical graphene sheets comprising a double-wall CN, using the macroscopic QED approach employed above to study the exciton-surface-plasmon interactions in single wall

nanotubes.⁶ The method is fully adequate in this case as the Casimir force is known to originate from quantum EM field fluctuations. The fundamental nature of this force has been studied for many years since the prediction of the attraction force between two neutral metallic plates in vacuum (see, Refs. [49, 56]). After the first report of observation of this spectacular effect [101], new measurements with improved accuracy have been done involving different geometries [102, 103, 104]. The Casimir force has also been considered theoretically with methods primarily based on the zero-point summation approach and Lifshitz theory [105, 106].

The Casimir effect has acquired a much broader impact recently due to its importance for nanostructured materials, including graphite and graphitic nanostructures [56] which can exist in different geometries and with various unique electronic properties. Moreover, the efficient development and operation of modern micro- and nano-electromechanical devices are limited due to effects such as stiction, friction, and adhesion, originating from or closely related to the Casimir effect [57].

The mechanisms governing the CN interactions still remain elusive. It is known that the system geometry [107, 108] and dielectric response [45, 62] have a profound effect on the interaction, in general, but their specific functionalities have not been qualitatively and quantitatively understood. Since CNs of virtually the same radial size can possess different electronic properties, investigating their Casimir interactions presents a unique opportunity to obtain insight into specific dielectric response features affecting the Casimir force between metallic and semiconducting cylindrical surfaces. This can also unveil the role of collective surface excitations in the energetic stability of multi-wall CNs of various chiral combinations.

Since Lifshitz theory cannot be easily applied to geometries other than parallel plates, researchers have used the Proximity Force Approximation (PFA) to calculate the Casimir interaction between CNs [107, 109] (see also Ref. [56] for the latest review). The method is based on approximating the curved surfaces at very close distances by a series of parallel plates and summing their energies using the Lifshitz result. Thus, the PFA is inherently an additive approach, applicable to objects at very close separations (still to be greater than objects inter-atomic distances) under the assumption that the CN dielectric response is the same as the one for the plates. This last assumption is very questionable as the quasi-1D character of the electronic motion in CNTs is known to be of principal importance for the correct description of their electronic and optical properties [1, 59, 64].

We model the double-wall CN by two infinitely long, infinitely thin, continuous concentric cylinders with radii $R_{1,2}$, immersed in vacuum. Each cylinder is characterized by the complex dynamic axial dielectric function $\epsilon_{zz}(R_{1,2}, \omega)$ with the z -direction along the CN axis as shown in Fig. 10. The azimuthal and radial components of the complete CN dielectric tensor are neglected as they are known to be much less than ϵ_{zz} for most CNs [64]. The QED quantization scheme in the presence

⁶In this Section only, the International System of units is used to make the comparison easier of our theory with other authors' results.

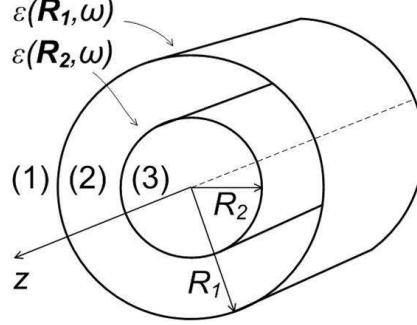


Figure 10: Schematic of the two concentric CNs in vacuum. The CN radii are R_1 and R_2 . The regions between the CN surfaces are denoted as (1), (2), and (3).

of CNs [49, 62] generates the second-quantized Hamiltonian

$$\hat{H} = \sum_{i=1,2} \int_0^\infty d\omega \hbar\omega \int d\mathbf{R}_i \hat{f}^\dagger(\mathbf{R}_i, \omega) \hat{f}(\mathbf{R}_i, \omega)$$

of the vacuum-type medium assisted EM field, with the bosonic operators \hat{f}^\dagger and \hat{f} creating and annihilating, respectively, surface EM excitations of frequency ω at points $\mathbf{R}_{1,2} = \{R_{1,2}, \varphi_{1,2}, z_{1,2}\}$ of the double-wall CN system. The Fourier-domain electric field operator at an arbitrary point $\mathbf{r} = (r, \varphi, z)$ is given by

$$\hat{E}(\mathbf{r}, \omega) = i\omega\mu_0 \sum_{i=1,2} \int d\mathbf{R}_i \mathbf{G}(\mathbf{r}, \mathbf{R}_i, \omega) \cdot \hat{\mathbf{J}}(\mathbf{R}_i, \omega),$$

where $\mathbf{G}(\mathbf{r}, \mathbf{R}_i, \omega)$ is the dyadic EM field Green's function (GF), and

$$\hat{\mathbf{J}}(\mathbf{R}_i, \omega) = \frac{\omega}{\mu_0 c^2} \sqrt{\frac{\hbar \text{Im} \epsilon_{zz}(R_i, \omega)}{\pi \epsilon_0}} \hat{f}(\mathbf{R}_i, \omega) \mathbf{e}_z$$

is the surface current density operator selected in such a way as to ensure the correct QED equal-time commutation relations for the electric and magnetic field operators [49, 62]. Here, \mathbf{e}_z is the unit vector along the CN axis, ϵ_0 , μ_0 , and c are the dielectric constant, magnetic permeability, and vacuum speed of light, respectively.

The dyadic GF satisfies the wave equation

$$\nabla \times \nabla \times \mathbf{G}(\mathbf{r}, \mathbf{r}', \omega) - \frac{\omega^2}{c^2} \mathbf{G}(\mathbf{r}, \mathbf{r}', \omega) = \delta(\mathbf{r} - \mathbf{r}') \mathbf{I} \quad (57)$$

with \mathbf{I} being the unit tensor. The GF can further be decomposed as follows

$$\mathbf{G}^{(s,f)} = \mathbf{G}^{(0)} \delta_{sf} + \mathbf{G}_{scatt}^{(s,f)}$$

where $\mathbf{G}^{(0)}$ and $\mathbf{G}_{scatt}^{(s,f)}$ represent the contributions of the direct and scattered waves, respectively [110, 111], with a point-like field source located in region s and the field registered in region f (see Fig. 10). The boundary conditions for Eq. (57) are obtained from those for the electric and magnetic field components on the CN surfaces [45, 59], which result in

$$\mathbf{e}_r \times \left[\mathbf{G}(\mathbf{r}, \mathbf{r}', \omega) \Big|_{R_{1,2}^+} - \mathbf{G}(\mathbf{r}, \mathbf{r}', \omega) \Big|_{R_{1,2}^-} \right] = 0, \quad (58)$$

$$\mathbf{e}_r \times \nabla \times \left[\mathbf{G}(\mathbf{r}, \mathbf{r}', \omega) \Big|_{R_{1,2}^+} - \mathbf{G}(\mathbf{r}, \mathbf{r}', \omega) \Big|_{R_{1,2}^-} \right] = i\omega\mu_0 \boldsymbol{\sigma}^{(1,2)}(\mathbf{r}, \omega) \cdot \mathbf{G}(\mathbf{r}, \mathbf{r}', \omega) \Big|_{R_{1,2}} \quad (59)$$

where \mathbf{e}_r is the unit vector along the radial direction. The discontinuity in Eq. (59) results from the full account of the finite absorption and dispersion for both CNs by means of their conductivity tensors $\boldsymbol{\sigma}^{(1,2)}$ approximated by their largest components

$$\sigma_{zz}^{(1,2)}(R_{1,2}, \omega) = -\frac{i\omega\epsilon_0}{S\rho_T} [\epsilon_{zz}^{(1,2)}(R_{1,2}, \omega) - 1] \quad (60)$$

[compare with Eq. (21)].

Following the procedure described in Refs. [110, 111], we expand $\mathbf{G}^{(0)}$ and $\mathbf{G}_{scatt}^{(s,f)}$ into series of even and odd vector cylindrical functions with unknown coefficients to be found from Eqs. (58) and (59). This splits the EM modes in the system into TE and TM polarizations, with Eqs. (58) and (59) yielding a set of 32 equations (16 for each polarization) with 32 unknown coefficients. The unknown coefficients are found determining the dyadic GF in each region.⁷

Using the expressions for the electric and magnetic fields, the electromagnetic stress tensor is constructed [49, 112]

$$\mathbf{T}(\mathbf{r}, \mathbf{r}') = \mathbf{T}_1(\mathbf{r}, \mathbf{r}') + \mathbf{T}_2(\mathbf{r}, \mathbf{r}') - \frac{1}{2} \mathbf{I} Tr [\mathbf{T}_1(\mathbf{r}, \mathbf{r}') + \mathbf{T}_2(\mathbf{r}, \mathbf{r}')] \quad (61)$$

$$\mathbf{T}_1(\mathbf{r}, \mathbf{r}') = \frac{\hbar}{\pi} \int_0^\infty d\omega \frac{\omega^2}{c^2} \text{Im} [\mathbf{G}(\mathbf{r}, \mathbf{r}', \omega)] \quad (62)$$

$$\mathbf{T}_2(\mathbf{r}, \mathbf{r}') = -\frac{\hbar}{\pi} \int_0^\infty d\omega \text{Im} \left[\nabla \times \mathbf{G}(\mathbf{r}, \mathbf{r}', \omega) \times \overleftarrow{\nabla}' \right] \quad (63)$$

We are interested in the radial component T_{rr} which describes the radiation pressure of the virtual EM field on each CN surface in the system. The Casimir force per unit area exerted on the surfaces is then given by [49]

$$F_i = \lim_{r \rightarrow R_i} \left\{ \lim_{\mathbf{r}' \rightarrow \mathbf{r}} \left[T_{rr}^{(i)}(\mathbf{r}, \mathbf{r}') - T_{rr}^{(i+1)}(\mathbf{r}, \mathbf{r}') \right] \right\}, \quad i = 1, 2 \quad (64)$$

⁷Due to the lengthy and tedious algebra, this derivation will be presented in a separate longer communication.

The forces $F_{1,2}$ calculated from Eq. (64) are of equal magnitude and opposite direction, indicating the attraction between the cylindrical surfaces. The Casimir force thus obtained accounts *simultaneously* for the geometrical curvature effects (through the GF tensor) and the finite absorption and dissipation of each CN [through their dielectric response functions (60)]. The dielectric response functions of particular CNs were calculated from the CN realistic band structure as described above, in Section 3. We decomposed them into the Drude contribution and the contribution originating from (transversely quantized) interband electronic transitions, $\epsilon_{zz} = \epsilon_{zz}^D + \epsilon_{zz}^{inter}$, in order to be able to see how much each individual contribution affects the inter-tube Casimir attraction.

It is interesting to consider the case of infinitely conducting parallel plates first using Eq. (64). This is obtained by taking the limits $\sigma_{zz}^{(1,2)} \rightarrow \infty$ and $R_{1,2} \rightarrow \infty$ while keeping constant the inter-tube distance, $R_1 - R_2 = d$. We find

$$F = -\frac{\hbar c}{16\pi^2 R_1^4} \int_0^\infty dx_1 x_1 \sum_{n=0}^\infty \frac{(2 - \delta_n^0)}{I_n(x_1)K_n(x_2) - I_n(x_2)K_n(x_1)}$$

$$\times \left\{ [x_1^2 K_n'^2(x_1) + (n^2 + x_1^2) K_n^2(x_1)] [I_n^2(x_1)K_n(x_2)/K_n(x_1) - 2I_n(x_1)I_n(x_2)] \right.$$

$$\left. - [x_1^2 I_n'^2(x_1) + (n^2 + x_1^2) I_n^2(x_1)] K_n(x_1)K_n(x_2) \right.$$

$$\left. - 2 [x_1^2 I_n'(x_1)K_n'(x_1) + (n^2 + x_1^2) I_n(x_1)K_n(x_1)] I_n(x_2)K_n(x_1) \right\}$$

where $x_{1,2} = xR_{1,2}$, $I_n(x)$ and $K_n(x)$ are the modified Bessel functions of the first and second kind, respectively. The above expression is obtained by making the transition to imaginary frequencies $\omega \rightarrow i\omega$, and using the Euclidean rotation technique as described in Refs. [112, 113]. This can further be evaluated by summing up the series over n using the large-order Bessel function expansions [114]. This results in $F \sim (-1/3)(\hbar c\pi^2/240d^4)$ which is 1/3 of the well-known result for two parallel plates [49, 56]. This deviation originates from $\epsilon_{zz} \neq 0$ only and the remaining dielectric tensor components being zero in our model.

Figure 11 presents results from the numerical calculations of F as a function of the inter-tube surface-to-surface distance for various pairs of CNs with their realistic chirality dependent dielectric responses taken into account. We have chosen the inner CN to be the achiral (12,12) metallic nanotube, and to change the outer tubes. As R_2 is varied, one can envision double wall CNs consisting of metal/metal or metal/semiconductor combinations of different chiralities but of similar radial dimensions.

Figure 11 shows that F decreases in strength as the surface-to-surface distance increases. This dependence is monotonic for the zigzag $(m, 0)$ and armchair (n, n) outer tubes, but it happens at different rates. The attraction is stronger if the outer CN is an armchair (n, n) one as compared to the attraction for the outer $(m, 0)$ nanotubes. At the same time, for chiral tubes the Casimir force decreases as a function of d in a rather irregular fashion. It is seen that for relatively small d ,

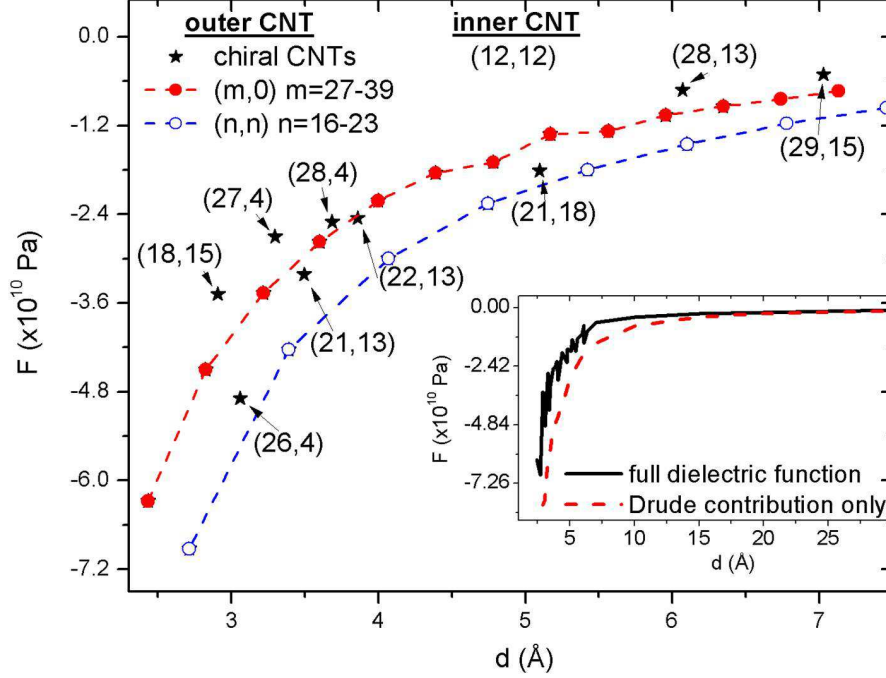


Figure 11: The Casimir force per unit area as a function of the inter-tube separation d , for different pairs of CNs. The inset shows force found with the full dielectric function and the Drude contribution only for the same CN pairs indicated in the figure.

the interaction force can be quite different. For example, the attraction between $(27, 4)@(12, 12)$ and $(21, 13)@(12, 12)$ differ by $\sim 20\%$ in favor of the second pair, even though the radial difference is only 0.2 \AA . The differences between the different CNs become smaller as their separation becomes larger, and they eventually become negligible as the Casimir force diminishes at large distances.

We also calculate the Casimir force using the $\epsilon_{zz}^D(\omega)$ contribution alone in each dielectric function. The inset in Fig. 11 indicates that the attraction is stronger when the interband transitions are neglected. The decay of F as a function of d is monotonic. Including the $\epsilon_{zz}^{inter}(\omega)$ term not only reduces the force, but also introduces non-linearities due to the chirality dependent optical excitations. At large surface-to-surface separations, the discrepancies between the force calculated with the full dielectric response, and those obtained with the Drude term only become less significant. We find that for $d \sim 15 \text{ \AA}$, this difference is less than 10% .

To investigate further the important functionalities originating from the cylindrical geometry and the CN dielectric response properties, F is calculated for different achiral inner/outer nanotube pairs. Studying zigzag and armchair CNs allows tracking generalities from $\epsilon(\omega)$ in a more controlled manner. The results are presented in

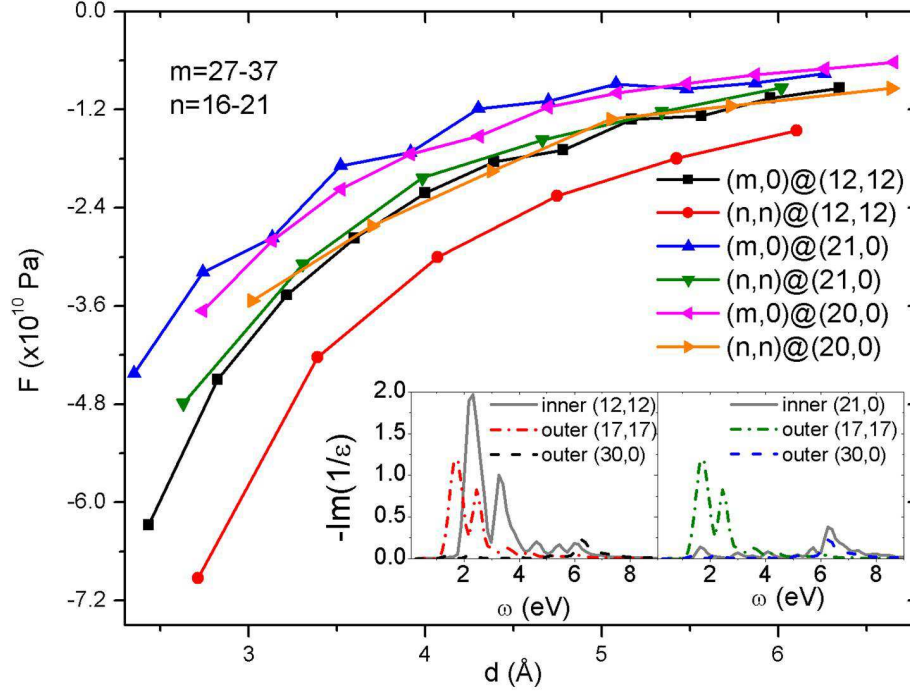


Figure 12: The Casimir force per unit area as a function of the inter-tube separation d for selected CN pairs. The insets show the EELS spectra for several CNs.

Fig. 12. We have chosen representatives of three inner CN types – metallic (12, 12), semi-metallic (21, 0), and semiconducting (20, 0) tubules. They are of similar radii, 8.14 Å, 8.22 Å, and 7.83 Å, respectively. We see that depending on the outer nanotube types, the F versus d curves are positioned in three groups. The weakest interaction is found when there are two zigzag concentric CNs (top two curves). The fact that some of these are semi-metallic and others are semiconducting does not seem to influence the magnitude and monotonic decrease of the Casimir force.

The attraction is stronger when there is a combination of an armchair and a zigzag CNT as compared to the previous case. The curves for $(m, 0)@(12, 12)$, $(n, n)@(21, 0)$, and $(n, n)@(20, 0)$ are practically overlapping, meaning that the specific location of the zigzag and armchair tubes (inner or outer) is of no significance to the force. The small deviations can be attributed to the small differences in the inner CN radii. Finally, we see that the strongest interaction occurs between two armchair CNs (red curve). These functionalities are not unique just for the considered CNs. We have performed the same calculations for many different achiral tubes, and we always find that the strongest interaction occurs between two armchair CNs and the weakest — between two zigzag CNs (provided that their radial dimensions are similar).

The results from these calculations are strongly suggestive that the CN collective excitation properties have a strong effect on their mutual interaction. This is particularly true for the relatively small distances of interest here, for which the dominant contribution of plasmonic modes to the Casimir interactions has been realized for planar [115] and linear [117] metallic systems. To elucidate this issue here, we calculate the EELS spectra, given by $-\text{Im}[1/\epsilon(\omega)]$, and compare them for various inner and outer CNs combinations — Fig. 12 (inset).

Considering F as a function of d and the specific form of the EELS spectra, it becomes clear from the inset in Fig. 12 that the low frequency plasmon excitations, given by peaks in $-\text{Im}[1/\epsilon(\omega)]$, are key to the strength of the Casimir force. We always find that the strongest force is between the tubules with well pronounced overlapping low frequency plasmon excitations. This is consistent with the conclusion of Ref. [117] for generic 1D-plasmonic structures. However, in our case we deal with the interband plasmons originating from the space quantization of the transverse electronic motion, and, therefore, having quite a different frequency-momentum dispersion law (constant) as compared to that normally assumed (linear) for plasmons [50]. A weaker force is obtained if only one of the CNs supports strong low frequency interband plasmon modes. The weakest interaction happens when neither CN has strong low frequency plasmons. For the cases shown in Fig 12, one finds well pronounced overlapping plasmon transitions in the (12, 12) CN at $\omega_1 = 2.18$ eV and $\omega_2 = 3.27$ eV, and at $\omega_1 = 1.63$ eV and $\omega_2 = 2.45$ eV in the (17, 17) CN. At the same time, no such well defined strong low frequency excitations in the (21, 0) and (30, 0) CNs are found. Figure 12 shows that the attraction in (17, 17)@(12, 12) is much stronger than the attraction in (30, 0)@(21, 0), even though the radial sizes of the involved CNs are approximately the same. One also notes that for the case of (17, 17)@(21, 0) there is only one such low frequency excitation coming from the armchair tube and, consequently, the Casimir force has an intermediate value as compared to the above discussed two cases.

We performed calculations of the Casimir force between many CN pairs and made comparisons between the relevant regions of the EELS spectra. It is found that, in general, armchair tubes always have strong, well pronounced interband plasmon excitations in the low frequency range. Zigzag and most chiral CNs have low frequency interband plasmons [37], too, but they are not as near as well pronounced as those in armchair tubes; their stronger plasmon modes are found at higher frequencies.

These studies are indicative of the significance of the collective response properties of the involved CNs. Specifically, the collective low energy plasmon excitations and their relative location can result in nanotube attraction with different strengths. We further investigate this point by considering a double wall CN with radii $R_1 = 11.63$ Å and $R_2 = 8.22$ Å. The dielectric function of each tube is taken

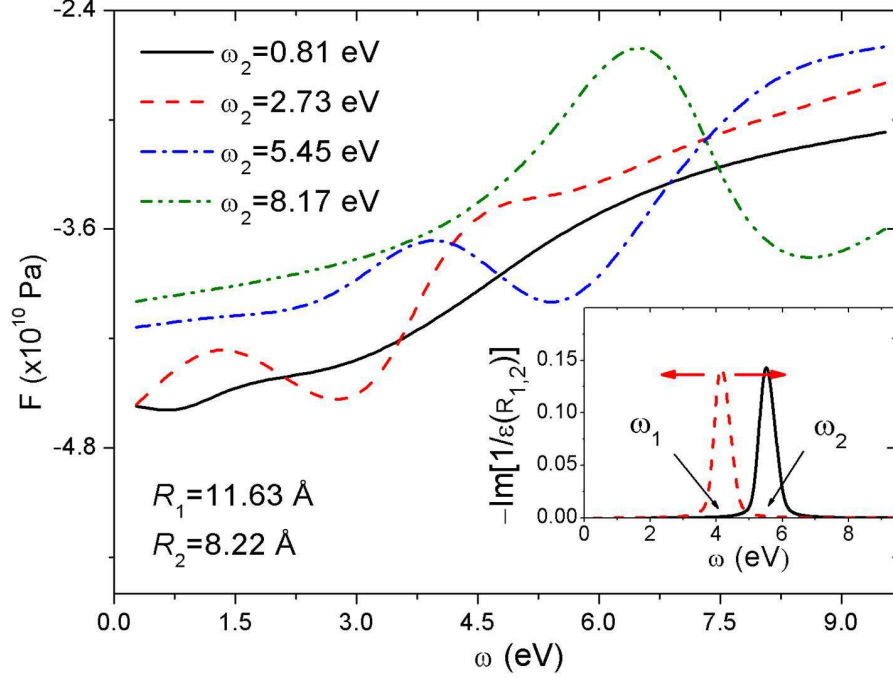


Figure 13: The Casimir force per unit area as a function of the outer CN plasmon frequency, while the inner CN plasmon peak ω_2 is constant. Results are shown for four values of ω_2 . The dielectric functions are modeled by a generic Lorentzian as given by Eq. (65).

to be of the generic Lorentzian form

$$\epsilon_{zz}(R_{1,2}, \omega) = 1 - \frac{\Omega^2}{\omega^2 - \omega_{1,2}^2 + i\omega\Gamma} \quad (65)$$

with the typical for nanotubes values $\Omega = 2.7$ eV and $\Gamma = 0.03$ eV [45]. Then, the EELS spectrum has only one plasmon resonance at $\omega_{1,2}$ for each tube. This generic form allows us to change the relative position and strength of the plasmon peaks and uncover more characteristic features originating from the EELS spectra.

In Fig. 13, the force as a function of plasmon frequency resonances of the outer CN is shown when the plasmon transition for the inner CNT is kept constant (four values are chosen for ω_2). One sees that the local minima in F versus ω occur when ω_1 and ω_2 coincide. In fact, the strongest attraction happens when both CNs have the lowest plasmon excitations at the same frequency $\omega_1 = \omega_2 = 0.81$ eV. It is evident that the existence of relatively strong low frequency EELS spectrum *and* an overlap between the relevant plasmon peaks of the two structures is necessary to achieve a strong interaction.

This study clearly demonstrates the crucial importance of the collective low energy surface plasmon excitations at relatively close surface-to-surface separations along with the cylindrical circular geometry of the double-wall CN system. The QED approach we used provides the unique opportunity to investigate these features together, or separately, and to uncover underlying mechanisms of the energetic stability of different double-wall CN combinations. An additional advantage here is that we can calculate the dielectric function explicitly for each chirality. Thus, we can determine unambiguously how the semiconducting or metallic nature of each CN contributes to their mutual interaction.

5 Conclusion

We have shown that the strong exciton-surface-plasmon coupling effect with characteristic exciton absorption line (Rabi) splitting ~ 0.1 eV exists in small-diameter ($\lesssim 1$ nm) semiconducting CNs. The splitting is almost as large as the typical exciton binding energies in such CNs ($\sim 0.3 - 0.8$ eV [19, 20, 24, 21]), and of the same order of magnitude as the exciton-plasmon Rabi splitting in organic semiconductors (~ 180 meV [53]). It is much larger than the exciton-polariton Rabi splitting in semiconductor microcavities ($\sim 140 - 400$ μ eV [81, 82, 83]), or the exciton-plasmon Rabi splitting in hybrid semiconductor-metal nanoparticle molecules [54].

Since the formation of the strongly coupled mixed exciton-plasmon excitations is only possible if the exciton total energy is in resonance with the energy of an interband surface plasmon mode, we have analyzed possible ways to tune the exciton energy to the nearest surface plasmon resonance. Specifically, the exciton energy may be tuned to the nearest plasmon resonance in ways used for the excitons in semiconductor quantum microcavities — thermally (by elevating sample temperature) [81, 82, 83], and/or electrostatically [84, 85, 86, 87] (via the quantum confined Stark effect with an external electrostatic field applied perpendicular to the CN axis). The two possibilities influence the different degrees of freedom of the quasi-1D exciton — the (longitudinal) kinetic energy and the excitation energy, respectively.

We have studied how the perpendicular electrostatic field affects the exciton excitation energy and interband plasmon resonance energy (the quantum confined Stark effect). Both of them are shown to shift to the red due to the decrease in the CN band gap as the field increases. However, the exciton red shift is much less than the plasmon one because of the decrease in the absolute value of the negative binding energy, which contributes largely to the exciton excitation energy. The exciton excitation energy and interband plasmon energy approach as the field increases, thereby bringing the total exciton energy in resonance with the plasmon mode due to the non-zero longitudinal kinetic energy term at finite temperature.

The noteworthy point is that the strong exciton-surface-plasmon coupling we predict here occurs in an individual CN as opposed to various artificially fabricated

hybrid plasmonic nanostructures mentioned above. We strongly believe this phenomenon, along with its tunability feature via the quantum confined Stark effect we have demonstrated, opens up new paths for the development of CN based tunable optoelectronic device applications in areas such as nanophotonics, nanoplasmonics, and cavity QED. One straightforward application like this is the CN photoluminescence control by means of the exciton-plasmon coupling tuned electrostatically via the quantum confined Stark effect. This complements the microcavity controlled CN infrared emitter application reported recently[27], offering the advantage of less stringent fabrication requirements at the same time since the planar photonic microcavity is no longer required. Electrostatically controlled coupling of two spatially separated (weakly localized) excitons to the same nanotube's plasmon resonance would result in their entanglement [11, 12, 13], the phenomenon that paves the way for CN based solid-state quantum information applications. Moreover, CNs combine advantages such as electrical conductivity, chemical stability, and high surface area that make them excellent potential candidates for a variety of more practical applications, including efficient solar energy conversion [7], energy storage [14], and optical nanobiosensorics [42]. However, the photoluminescence quantum yield of individual CNs is relatively low, and this hinders their uses in the aforementioned applications. CN bundles and films are proposed to be used to surpass the poor performance of individual tubes. The theory of the exciton-plasmon coupling we have developed here, being extended to include the inter-tube interaction, complements currently available 'weak-coupling' theories of the exciton-plasmon interactions in low-dimensional nanostructures [54, 121] with the very important case of the strong coupling regime. Such an extended theory (subject of our future publication) will lay the foundation for understanding inter-tube energy transfer mechanisms that affect the efficiency of optoelectronic devices made of CN bundles and films, as well as it will shed more light on the recent photoluminescence experiments with CN bundles [43, 44] and multi-walled CNs [122], revealing their potentialities for the development of high-yield, high-performance optoelectronics applications with CNs.

In addition, we have first applied the macroscopic QED approach suitable for dispersing and absorbing media to study the Casimir interaction in a double-wall carbon nanotube systems with the realistic dielectric response taken into account. We found that at distances similar to the equilibrium separations between graphitic surfaces ($\sim 3 \text{ \AA}$), the attraction is dominated by the low energy (interband) plasmon excitations of both CNs. The key attributes of the EELS spectra are the existence of low frequency plasmons, their strong and well pronounced nature, and the overlap between the low frequency plasmon peaks belonging to the two CNTs. Thus, the chiralities of concentric graphene sheets with similar radial sizes exhibiting these features will be responsible for forming the most preferred CN pairs. As the inter-tube separation increases, the plasmon effect diminishes and the collective excitations originating from the nanotube metallic or semiconducting nature do not influence the interaction in a profound way.

We expect our results to pave the way for the development of new generation of tunable optoelectronic and nano-electromechanical device applications with single-wall and multi-wall carbon nanotubes.

Acknowledgements

I.V.B. is supported by the US National Science Foundation, Army Research Office and NASA (grants ECCS-1045661 & HRD-0833184, W911NF-10-1-0105, and NNX09AV07A). L.M.W. and A.P. are supported by the US Department of Energy contract DE-FG02-06ER46297. Helpful discussions with Mikhail Braun (St.-Peterburg U., Russia), Jonathan Finley (WSI, TU Munich, Germany), and Alexander Govorov (Ohio U., USA) are gratefully acknowledged.

Appendix A

Exciton interaction with the surface EM field

We follow our recently developed QED formalism to describe vacuum-type EM effects in the presence of quasi-1D absorbing and dispersive bodies [58, 59, 60, 61, 62, 9]. The treatment begins with the most general EM interaction of the surface charge fluctuations with the quantized surface EM field of a single-walled CN. No external field is assumed to be applied. The CN is modelled by a neutral, infinitely long, infinitely thin, anisotropically conducting cylinder. Only the axial conductivity of the CN, σ_{zz} , is taken into account, whereas the azimuthal one, $\sigma_{\varphi\varphi}$, is neglected being strongly suppressed by the transverse depolarization effect [63, 64, 65, 66, 67, 68]. Since the problem has the cylindrical symmetry, the orthonormal cylindrical basis $\{\mathbf{e}_r, \mathbf{e}_\varphi, \mathbf{e}_z\}$ is used with the vector \mathbf{e}_z directed along the nanotube axis as shown in Fig. 1. The interaction has the following form (Gaussian system of units)

$$\begin{aligned} \hat{H}_{int} &= \hat{H}_{int}^{(1)} + \hat{H}_{int}^{(2)} \\ &= - \sum_{\mathbf{n}, i} \frac{q_i}{m_i c} \hat{\mathbf{A}}(\mathbf{n} + \hat{\mathbf{r}}_{\mathbf{n}}^{(i)}) \cdot \left[\hat{\mathbf{p}}_{\mathbf{n}}^{(i)} - \frac{q_i}{2c} \hat{\mathbf{A}}(\mathbf{n} + \hat{\mathbf{r}}_{\mathbf{n}}^{(i)}) \right] + \sum_{\mathbf{n}, i} q_i \hat{\varphi}(\mathbf{n} + \hat{\mathbf{r}}_{\mathbf{n}}^{(i)}), \end{aligned} \quad (66)$$

where c is the speed of light, m_i , q_i , $\hat{\mathbf{r}}_{\mathbf{n}}^{(i)}$, and $\hat{\mathbf{p}}_{\mathbf{n}}^{(i)}$ are, respectively, the masses, charges, coordinate operators and momenta operators of the particles (electrons and nucleus) residing at the lattice site $\mathbf{n} = \mathbf{R}_{\mathbf{n}} = \{R_{CN}, \varphi_n, z_n\}$ associated with a carbon atom (see Fig. 1) on the surface of the CN of radius R_{CN} . The summation is taken over the lattice sites, and may be substituted with the integration over the CN surface using Eq. (3). The vector potential operator $\hat{\mathbf{A}}$ and the scalar potential operator $\hat{\varphi}$ represent the nanotube's transversely polarized and longitudinally polarized surface EM modes, respectively. They are written in the Schrödinger picture

as follows

$$\hat{\mathbf{A}}(\mathbf{n}) = \int_0^\infty d\omega \frac{c}{i\omega} \hat{\underline{\mathbf{E}}}^\perp(\mathbf{n}, \omega) + h.c., \quad (67)$$

$$-\nabla_{\mathbf{n}} \hat{\varphi}(\mathbf{n}) = \int_0^\infty d\omega \hat{\underline{\mathbf{E}}}^\parallel(\mathbf{n}, \omega) + h.c.. \quad (68)$$

We use the Coulomb gauge whereby $\nabla_{\mathbf{n}} \cdot \hat{\mathbf{A}}(\mathbf{n}) = 0$, or $[\hat{\mathbf{p}}_{\mathbf{n}}^{(i)}, \hat{\mathbf{A}}(\mathbf{n} + \hat{\mathbf{r}}_{\mathbf{n}}^{(i)})] = 0$.

The total electric field operator of the CN-modified EM field is given for an arbitrary \mathbf{r} in the Schrödinger picture by

$$\hat{\mathbf{E}}(\mathbf{r}) = \int_0^\infty d\omega \hat{\underline{\mathbf{E}}}(\mathbf{r}, \omega) + h.c. = \int_0^\infty d\omega [\hat{\underline{\mathbf{E}}}^\perp(\mathbf{r}, \omega) + \hat{\underline{\mathbf{E}}}^\parallel(\mathbf{r}, \omega)] + h.c. \quad (69)$$

with the transversely (longitudinally) polarized Fourier-domain field components defined as

$$\hat{\underline{\mathbf{E}}}^{\perp(\parallel)}(\mathbf{r}, \omega) = \int d\mathbf{r}' \delta^{\perp(\parallel)}(\mathbf{r} - \mathbf{r}') \cdot \hat{\underline{\mathbf{E}}}(\mathbf{r}', \omega), \quad (70)$$

where

$$\delta_{\alpha\beta}^\parallel(\mathbf{r}) = -\nabla_\alpha \nabla_\beta \frac{1}{4\pi r}, \quad (71)$$

$$\delta_{\alpha\beta}^\perp(\mathbf{r}) = \delta_{\alpha\beta} \delta(\mathbf{r}) - \delta_{\alpha\beta}^\parallel(\mathbf{r})$$

are the longitudinal and transverse dyadic δ -functions, respectively. The total field operator (69) satisfies the set of the Fourier-domain Maxwell equations

$$\nabla \times \hat{\underline{\mathbf{E}}}(\mathbf{r}, \omega) = ik \hat{\underline{\mathbf{H}}}(\mathbf{r}, \omega), \quad (72)$$

$$\nabla \times \hat{\underline{\mathbf{H}}}(\mathbf{r}, \omega) = -ik \hat{\underline{\mathbf{E}}}(\mathbf{r}, \omega) + \frac{4\pi}{c} \hat{\underline{\mathbf{I}}}(\mathbf{r}, \omega), \quad (73)$$

where $\hat{\underline{\mathbf{H}}} = (ik)^{-1} \nabla \times \hat{\underline{\mathbf{E}}}$ is the magnetic field operator, $k = \omega/c$, and

$$\hat{\underline{\mathbf{I}}}(\mathbf{r}, \omega) = \sum_{\mathbf{n}} \delta(\mathbf{r} - \mathbf{n}) \hat{\underline{\mathbf{J}}}(\mathbf{n}, \omega), \quad (74)$$

is the exterior current operator with the current density defined as follows

$$\hat{\underline{\mathbf{J}}}(\mathbf{n}, \omega) = \sqrt{\frac{\hbar\omega \operatorname{Re}\sigma_{zz}(R_{CN}, \omega)}{\pi}} \hat{f}(\mathbf{n}, \omega) \mathbf{e}_z \quad (75)$$

to ensure preservation of the fundamental QED equal-time commutation relations (see, e.g., [47]) for the EM field components in the presence of a CN. Here, σ_{zz} is the CN surface axial conductivity per unit length, and $\hat{f}(\mathbf{n}, \omega)$ along with its counterpart $\hat{f}^\dagger(\mathbf{n}, \omega)$ are the scalar bosonic field operators which annihilate and create,

respectively, single-quantum EM field excitations of frequency ω at the lattice site \mathbf{n} of the CN surface. They satisfy the standard bosonic commutation relations

$$[\hat{f}(\mathbf{n}, \omega), \hat{f}^\dagger(\mathbf{m}, \omega')] = \delta_{\mathbf{n}\mathbf{m}} \delta(\omega - \omega'), \quad (76)$$

$$[\hat{f}(\mathbf{n}, \omega), \hat{f}(\mathbf{m}, \omega')] = [\hat{f}^\dagger(\mathbf{n}, \omega), \hat{f}^\dagger(\mathbf{m}, \omega')] = 0.$$

One further obtains from Eqs. (72)–(75) that

$$\hat{\mathbf{E}}(\mathbf{r}, \omega) = ik \frac{4\pi}{c} \sum_{\mathbf{n}} \mathbf{G}(\mathbf{r}, \mathbf{n}, \omega) \cdot \hat{\mathbf{J}}(\mathbf{n}, \omega), \quad (77)$$

and, according to Eqs. (69) and (70),

$$\hat{\mathbf{E}}^{\perp(\parallel)}(\mathbf{r}, \omega) = ik \frac{4\pi}{c} \sum_{\mathbf{n}} {}^{\perp(\parallel)}\mathbf{G}(\mathbf{r}, \mathbf{n}, \omega) \cdot \hat{\mathbf{J}}(\mathbf{n}, \omega), \quad (78)$$

where ${}^{\perp}\mathbf{G}$ and ${}^{\parallel}\mathbf{G}$ are the transverse part and the longitudinal part, respectively, of the total Green tensor $\mathbf{G} = {}^{\perp}\mathbf{G} + {}^{\parallel}\mathbf{G}$ of the classical EM field in the presence of the CN. This tensor satisfies the equation

$$\sum_{\alpha=r,\varphi,z} (\nabla \times \nabla \times - k^2)_{z\alpha} G_{\alpha z}(\mathbf{r}, \mathbf{n}, \omega) = \delta(\mathbf{r} - \mathbf{n}) \quad (79)$$

together with the radiation conditions at infinity and the boundary conditions on the CN surface.

All the 'discrete' quantities in Eqs. (74)–(79) may be equivalently rewritten in continuous variables in view of Eq. (3). Being applied to the identity $1 = \sum_{\mathbf{m}} \delta_{\mathbf{n}\mathbf{m}}$, Eq. (3) yields

$$\delta_{\mathbf{n}\mathbf{m}} = S_0 \delta(\mathbf{R}_n - \mathbf{R}_m). \quad (80)$$

This requires to redefine

$$\hat{f}(\mathbf{n}, \omega) = \sqrt{S_0} \hat{f}(\mathbf{R}_n, \omega), \quad \hat{f}^\dagger(\mathbf{n}, \omega) = \sqrt{S_0} \hat{f}^\dagger(\mathbf{R}_n, \omega) \quad (81)$$

in the commutation relations (76). Similarly, from Eq. (77), in view of Eqs. (3), (75) and (81), one obtains

$$\mathbf{G}(\mathbf{r}, \mathbf{n}, \omega) = \sqrt{S_0} \mathbf{G}(\mathbf{r}, \mathbf{R}_n, \omega), \quad (82)$$

which is also valid for the transverse and longitudinal Green tensors in Eq. (78).

Next, we make the series expansions of the interactions $\hat{H}_{int}^{(1)}$ and $\hat{H}_{int}^{(2)}$ in Eq. (66) about the lattice site \mathbf{n} to the first non-vanishing terms,

$$\hat{H}_{int}^{(1)} \approx - \sum_{\mathbf{n}, i} \frac{q_i}{m_i c} \hat{\mathbf{A}}(\mathbf{n}) \cdot \hat{\mathbf{p}}_{\mathbf{n}}^{(i)} + \sum_{\mathbf{n}, i} \frac{q_i^2}{2m_i c^2} \hat{\mathbf{A}}^2(\mathbf{n}), \quad (83)$$

$$\hat{H}_{int}^{(2)} \approx \sum_{\mathbf{n}, i} q_i \nabla_{\mathbf{n}} \hat{\varphi}(\mathbf{n}) \cdot \hat{\mathbf{r}}_{\mathbf{n}}^{(i)}, \quad (84)$$

and introduce the single-lattice-site Hamiltonian

$$\hat{H}_{\mathbf{n}} = \varepsilon_0 |0\rangle\langle 0| + \sum_f (\varepsilon_0 + \hbar\omega_f) |f\rangle\langle f| \quad (85)$$

with the completeness relation

$$|0\rangle\langle 0| + \sum_f |f\rangle\langle f| = \hat{I}. \quad (86)$$

Here, ε_0 is the energy of the ground state $|0\rangle$ (no exciton excited) of the carbon atom associated with the lattice site \mathbf{n} , $\varepsilon_0 + \hbar\omega_f$ is the energy of the excited carbon atom in the quantum state $|f\rangle$ with one f -internal-state exciton formed of the energy $E_{exc}^{(f)} = \hbar\omega_f$. In view of Eqs. (85) and (86), one has

$$\begin{aligned} \hat{\mathbf{p}}_{\mathbf{n}}^{(i)} &= m_i \frac{d\hat{\mathbf{r}}_{\mathbf{n}}^{(i)}}{dt} = \frac{m_i}{i\hbar} [\hat{\mathbf{r}}_{\mathbf{n}}^{(i)}, \hat{H}_{\mathbf{n}}] = \frac{m_i}{i\hbar} \hat{I} [\hat{\mathbf{r}}_{\mathbf{n}}^{(i)}, \hat{H}_{\mathbf{n}}] \hat{I} \\ &\approx \frac{m_i}{i\hbar} \sum_f \hbar\omega_f \left(\langle 0 | \hat{\mathbf{r}}_{\mathbf{n}}^{(i)} | f \rangle B_{\mathbf{n},f} - \langle f | \hat{\mathbf{r}}_{\mathbf{n}}^{(i)} | 0 \rangle B_{\mathbf{n},f}^\dagger \right) \end{aligned} \quad (87)$$

and

$$\hat{\mathbf{r}}_{\mathbf{n}}^{(i)} = \hat{I} \hat{\mathbf{r}}_{\mathbf{n}}^{(i)} \hat{I} \approx \sum_f \left(\langle 0 | \hat{\mathbf{r}}_{\mathbf{n}}^{(i)} | f \rangle B_{\mathbf{n},f} + \langle f | \hat{\mathbf{r}}_{\mathbf{n}}^{(i)} | 0 \rangle B_{\mathbf{n},f}^\dagger \right), \quad (88)$$

where $\langle 0 | \hat{\mathbf{r}}_{\mathbf{n}}^{(i)} | f \rangle = \langle f | \hat{\mathbf{r}}_{\mathbf{n}}^{(i)} | 0 \rangle$ in view of the hermitian and real character of the coordinate operator. The operators $B_{\mathbf{n},f} = |0\rangle\langle f|$ and $B_{\mathbf{n},f}^\dagger = |f\rangle\langle 0|$ create and annihilate, respectively, the f -internal-state exciton at the lattice site \mathbf{n} , and exciton-to-exciton transitions are neglected. In addition, we also have

$$\delta_{ij} \delta_{\alpha\beta} = \frac{i}{\hbar} [(\hat{\mathbf{p}}_{\mathbf{n}}^{(i)})_\alpha, (\hat{\mathbf{r}}_{\mathbf{n}}^{(j)})_\beta], \quad (89)$$

where $\alpha, \beta = r, \varphi, z$. Substituting these into Eqs. (83) and (84) [commutator (89) goes into the second term of Eq. (83) which is to be pre-transformed as follows $\sum_{i,j,\alpha,\beta} q_i q_j \hat{A}(\mathbf{n})_\alpha \hat{A}(\mathbf{n})_\beta \delta_{ij} \delta_{\alpha\beta} / 2m_i c^2$], one arrives at the following (electric dipole) approximation of Eq. (66)

$$\begin{aligned} \hat{H}_{int} &= \hat{H}_{int}^{(1)} + \hat{H}_{int}^{(2)} \\ &= - \sum_{\mathbf{n},f} \frac{i\omega_f}{c} \mathbf{d}_{\mathbf{n}}^f \cdot \hat{\mathbf{A}}(\mathbf{n}) \left[B_{\mathbf{n},f}^\dagger - B_{\mathbf{n},f} + \frac{i}{\hbar c} \mathbf{d}_{\mathbf{n}}^f \cdot \hat{\mathbf{A}}(\mathbf{n}) \right] \\ &\quad + \sum_{\mathbf{n},f} \mathbf{d}_{\mathbf{n}}^f \cdot \nabla_{\mathbf{n}} \hat{\varphi}(\mathbf{n}) \left(B_{\mathbf{n},f}^\dagger + B_{\mathbf{n},f} \right) \end{aligned} \quad (90)$$

with $\mathbf{d}_n^f = \langle 0 | \hat{\mathbf{d}}_n | f \rangle = \langle f | \hat{\mathbf{d}}_n | 0 \rangle$, where $\hat{\mathbf{d}}_n = \sum_i q_i \hat{\mathbf{r}}_n^{(i)}$ is the total electric dipole moment operator of the particles residing at the lattice site \mathbf{n} .

The Hamiltonian (90) is seen to describe the vacuum-type exciton interaction with the surface EM field (created by the charge fluctuations on the nanotube surface). The last term in the square brackets does not depend on the exciton operators, and therefore results in the constant energy shift which can be safely neglected. We then arrive, after using Eqs. (67), (68), (75), and (78), at the following second quantized interaction Hamiltonian

$$\hat{H}_{int} = \sum_{\mathbf{n}, \mathbf{m}, f} \int_0^\infty d\omega [g_f^{(+)}(\mathbf{n}, \mathbf{m}, \omega) B_{\mathbf{n}, f}^\dagger - g_f^{(-)}(\mathbf{n}, \mathbf{m}, \omega) B_{\mathbf{n}, f}] \hat{f}(\mathbf{m}, \omega) + h.c., \quad (91)$$

where

$$g_f^{(\pm)}(\mathbf{n}, \mathbf{m}, \omega) = g_f^\perp(\mathbf{n}, \mathbf{m}, \omega) \pm \frac{\omega}{\omega_f} g_f^\parallel(\mathbf{n}, \mathbf{m}, \omega) \quad (92)$$

with

$$g_f^{\perp(\parallel)}(\mathbf{n}, \mathbf{m}, \omega) = -i \frac{4\omega_f}{c^2} \sqrt{\pi \hbar \omega \operatorname{Re} \sigma_{zz}(R_{CN}, \omega)} \sum_{\alpha=r, \varphi, z} (\mathbf{d}_n^f)_\alpha \perp(\parallel) G_{\alpha z}(\mathbf{n}, \mathbf{m}, \omega), \quad (93)$$

and

$$\perp(\parallel) G_{\alpha z}(\mathbf{n}, \mathbf{m}, \omega) = \int d\mathbf{r} \delta_{\alpha\beta}^{\perp(\parallel)}(\mathbf{n} - \mathbf{r}) G_{\beta z}(\mathbf{r}, \mathbf{m}, \omega). \quad (94)$$

This yields Eqs. (10)–(12) after the strong transverse depolarization effect in CNs is taken into account whereby $\mathbf{d}_n^f \approx (\mathbf{d}_n^f)_z \mathbf{e}_z$.

Appendix B

Green tensor of the surface EM field

Within the model of an infinitely thin, infinitely long, anisotropically conducting cylinder we utilize here, the classical EM field Green tensor is found by expanding the solution to the Green equation (79) in series in cylindrical coordinates, and then imposing the appropriately chosen boundary conditions on the CN surface to determine the Wronskian normalization constant (see, e.g., Ref. [118]).

After the EM field is divided into the transversely and longitudinally polarized components according to Eqs. (69)–(71), the Green equation (79) takes the form

$$\sum_{\alpha=r, \varphi, z} (\nabla \times \nabla \times - k^2)_{z\alpha} \left[\perp G_{\alpha z}(\mathbf{r}, \mathbf{n}, \omega) + \parallel G_{\alpha z}(\mathbf{r}, \mathbf{n}, \omega) \right] = \delta(\mathbf{r} - \mathbf{n}) \quad (95)$$

with the two additional constraints,

$$\sum_{\alpha=r, \varphi, z} \nabla_\alpha \perp G_{\alpha z}(\mathbf{r}, \mathbf{n}, \omega) = 0 \quad (96)$$

and

$$\sum_{\beta,\gamma=r,\varphi,z} \epsilon_{\alpha\beta\gamma} \nabla_{\beta} \parallel G_{\gamma z}(\mathbf{r}, \mathbf{n}, \omega) = 0, \quad (97)$$

where $\epsilon_{\alpha\beta\gamma}$ is the totally antisymmetric unit tensor of rank 3. Equations (96) and (97) originate from the divergence-less character (Coulomb gauge) of the transverse EM component and the curl-less character of the longitudinal EM component, respectively. The transverse ${}^{\perp}G_{\alpha z}$ and longitudinal $\parallel G_{\alpha z}$ Green tensor components are defined by Eq. (94) which is the corollary of Eq. (70) using the Eqs. (77) and (78). Equation (95) is further rewritten in view of Eqs. (96) and (97), to give the following two independent equations for ${}^{\perp}G_{zz}$ and $\parallel G_{zz}$ we need

$$(\Delta + k^2) {}^{\perp}G_{zz}(\mathbf{r}, \mathbf{n}, \omega) = -\delta_{zz}^{\perp}(\mathbf{r} - \mathbf{n}), \quad (98)$$

$$k^2 \parallel G_{zz}(\mathbf{r}, \mathbf{n}, \omega) = -\delta_{zz}^{\parallel}(\mathbf{r} - \mathbf{n}) \quad (99)$$

with the transverse and longitudinal delta-functions defined by Eq. (71).

We use the differential representations for the transverse ${}^{\perp}G_{zz}$ and longitudinal $\parallel G_{zz}$ Green functions of the following form [consistent with Eq. (94)]

$${}^{\perp}G_{zz}(\mathbf{r}, \mathbf{n}, \omega) = \left(\frac{1}{k^2} \nabla_z \nabla_z + 1 \right) g(\mathbf{r}, \mathbf{n}, \omega), \quad (100)$$

$$\parallel G_{zz}(\mathbf{r}, \mathbf{n}, \omega) = -\frac{1}{k^2} \nabla_z \nabla_z g(\mathbf{r}, \mathbf{n}, \omega), \quad (101)$$

where $g(\mathbf{r}, \mathbf{n}, \omega)$ is the scalar Green function of the Helmholtz equation (98), satisfying the radiation condition at infinity and the finiteness condition on the axis of the cylinder. Such a function is known to be given by the following series expansion

$$g(\mathbf{r}, \mathbf{n}, \omega) = \frac{\sqrt{S_0}}{4\pi} \frac{e^{ik|\mathbf{r}-\mathbf{R}_n|}}{|\mathbf{r}-\mathbf{R}_n|} = \frac{\sqrt{S_0}}{(2\pi)^2} \sum_{p=-\infty}^{\infty} e^{ip(\varphi-\varphi_n)} \quad (102)$$

$$\times \int_C dh I_p(vr) K_p(vR_{CN}) e^{ih(z-z_n)}, \quad r \leq R_{CN},$$

where I_p and K_p are the modified cylindric Bessel functions, $v = v(h, \omega) = \sqrt{h^2 - k^2}$, and we used the property (82) to go from the discrete variable \mathbf{n} to the corresponding continuous variable. The integration contour C goes along the real axis of the complex plane and envelopes the branch points $\pm k$ of the integrand from below and from above, respectively. For $r \geq R_{CN}$, the function $g(\mathbf{r}, \mathbf{n}, \omega)$ is obtained from Eq. (102) by means of a simple symbol replacement $I_p \leftrightarrow K_p$ in the integrand.

The scalar function (102) is to be imposed the boundary conditions on the CN surface. To derive them, we represent the classical electric and magnetic field com-

ponents in terms of the EM field Green tensor as follows

$$\underline{E}_\alpha(\mathbf{r}, \omega) = ik^\perp G_{\alpha z}(\mathbf{r}, \mathbf{n}, \omega), \quad (103)$$

$$\underline{H}_\alpha(\mathbf{r}, \omega) = -\frac{i}{k} \sum_{\beta, \gamma=r, \varphi, z} \epsilon_{\alpha\beta\gamma} \nabla_\beta E_\gamma(\mathbf{r}, \omega). \quad (104)$$

These are valid for $\mathbf{r} \neq \mathbf{n}$ under the Coulomb-gauge condition. The boundary conditions are then obtained from the standard requirements that the tangential electric field components be continuous across the surface, and the tangential magnetic field components be discontinuous by an amount proportional to the free surface current density, which we approximate here by the (strongest) *axial* component, $\sigma_{zz}(R_{CN}, \omega)$, of the nanotube's surface conductivity. Under this approximation, one has

$$\underline{E}_z|_+ - \underline{E}_z|_- = \underline{E}_\varphi|_+ - \underline{E}_\varphi|_- = 0, \quad (105)$$

$$\underline{H}_z|_+ - \underline{H}_z|_- = 0, \quad (106)$$

$$\underline{H}_\varphi|_+ - \underline{H}_\varphi|_- = \frac{4\pi}{c} \sigma_{zz}(\omega) \underline{E}_z|_{R_{CN}}, \quad (107)$$

where \pm stand for $r = R_{CN} \pm \varepsilon$ with the positive infinitesimal ε . In view of Eqs. (103), (104) and (100), the boundary conditions above result in the following two boundary conditions for the function (102)

$$g|_+ - g|_- = 0, \quad (108)$$

$$\left. \frac{\partial g}{\partial r} \right|_+ - \left. \frac{\partial g}{\partial r} \right|_- = -\frac{4\pi i \sigma_{zz}(\omega)}{\omega} \left(\frac{\partial^2}{\partial z^2} + k^2 \right) g|_{R_{CN}}. \quad (109)$$

We see that Eq. (108) is satisfied identically. Eq. (109) yields the Wronskian of modified Bessel functions on the left, $W[I_p(x), K_p(x)] = I_p(x)K_p'(x) - K_p(x)I_p'(x) = -1/x$, which brings us to the equation

$$-\frac{1}{R_{CN}} = \frac{4\pi i \sigma_{zz}(\omega)}{\omega} v^2 I_p(vR_{CN}) K_p(vR_{CN}). \quad (110)$$

This is nothing but the dispersion relation which determines the radial wave numbers, h , of the CN surface EM modes with given p and ω . Since we are interested here in the EM field Green tensor on the CN surface [see Eq. (93)], not in particular surface EM modes, we substitute $I_p(vR_{CN})K_p(vR_{CN})$ from Eq. (110) into Eq. (102) with $r = R_{CN}$. This allows us to obtain the scalar Green function of interest with the boundary conditions (108) and (109) taken into account. We have

$$g(\mathbf{R}, \mathbf{n}, \omega) = -\frac{i\omega\sqrt{S_0} \delta(\varphi - \varphi_n)}{8\pi^2 \sigma_{zz}(\omega) R_{CN}} \int_C dh \frac{e^{ih(z-z_n)}}{k^2 - h^2}, \quad (111)$$

where $\mathbf{R} = \{R_{CN}, \varphi, z\}$ is an arbitrary point of the cylindrical surface. Using further the residue theorem to calculate the contour integral, we arrive at the final expression of the form

$$g(\mathbf{R}, \mathbf{n}, \omega) = -\frac{c\sqrt{S_0}\delta(\varphi - \varphi_n)}{8\pi\sigma_{zz}(\omega)R_{CN}} e^{i\omega|z-z_n|/c}, \quad (112)$$

which yields

$${}^\perp G_{zz}(\mathbf{R}, \mathbf{n}, \omega) \equiv 0, \quad (113)$$

$${}^\parallel G_{zz}(\mathbf{R}, \mathbf{n}, \omega) = g(\mathbf{R}, \mathbf{n}, \omega), \quad (114)$$

in view of Eqs. (100) and (101).

The fact that the transverse Green function (113) identically equals zero on the CN surface is related to the absence of the skin layer in the model of the infinitely thin cylinder (see, e.g., Ref. [118]). In this model, the transverse Green function is only non-zero in the near-surface area where the exciton wave function goes to zero. Thus, only longitudinally polarized EM modes with the Green function (114) contribute to the exciton surface EM field interaction on the nanotube surface.

Appendix C

Diagonalization of the Hamiltonian (1)–(13)

We start with the transformation of the total Hamiltonian (1)–(13) to the \mathbf{k} -representation using Eqs. (5) and (9). The unperturbed part presents no difficulties. Special care should be given to the interaction matrix element $g_f^{(\pm)}(\mathbf{n}, \mathbf{m}, \omega)$ in Eq. (13). In view of Eqs. (114), (112) and (3), one has explicitly

$$\begin{aligned} g_f^{(\pm)}(\mathbf{k}, \mathbf{k}', \omega) &= \frac{1}{N} \sum_{\mathbf{n}, \mathbf{m}} g_f^{(\pm)}(\mathbf{n}, \mathbf{m}, \omega) e^{-i\mathbf{k}\cdot\mathbf{n} + i\mathbf{k}'\cdot\mathbf{m}} \\ &= \pm \frac{i\omega\sqrt{\pi\hbar\omega} \operatorname{Re} \sigma_{zz}(\omega)}{2\pi c \sigma_{zz}(\omega) R_{CN}} \frac{d_z^f}{N} \sqrt{S_0} \frac{R_{CN}^2}{N S_0^2} \\ &\times \int_0^{2\pi} d\varphi_n d\varphi_m \delta(\varphi_n - \varphi_m) e^{-ik_\varphi\varphi_n + ik'_\varphi\varphi_m} \int_{-\infty}^{\infty} dz_n dz_m e^{i\omega|z_n - z_m|/c - ik_z z_n + ik'_z z_m}, \end{aligned} \quad (115)$$

where we have also taken into account the fact that the dipole matrix element $(\mathbf{d}_n^f)_z = \langle 0 | (\hat{\mathbf{d}}_n)_z | f \rangle$ is the same for all the lattice sites on the CN surface in view of their equivalence. As a consequence, $(\mathbf{d}_n^f)_z = d_z^f/N$ with $d_z^f = \sum_{\mathbf{n}} \langle 0 | (\hat{\mathbf{d}}_n)_z | f \rangle$.

The integral over φ in Eq. (115) is taken in a standard way to yield

$$\int_0^{2\pi} d\varphi_n d\varphi_m \delta(\varphi_n - \varphi_m) e^{-ik_\varphi\varphi_n + ik'_\varphi\varphi_m} = 2\pi \delta_{k_\varphi k'_\varphi}. \quad (116)$$

The integration over z is performed by first writing the integral in the form

$$\int_{-\infty}^{\infty} dz_n dz_m \dots = \lim_{L \rightarrow \infty} \int_{-L/2}^{L/2} dz_n \int_{-L/2}^{L/2} dz_m \dots$$

(L being the CN length), then dividing it into two parts by means of the equation

$$e^{i\omega|z_n - z_m|/c} = \theta(z_n - z_m) e^{i\omega(z_n - z_m)/c} + \theta(z_m - z_n) e^{-i\omega(z_n - z_m)/c},$$

and finally by taking simple exponential integrals with allowance made for the formula

$$\delta_{k_z k'_z} = \lim_{L \rightarrow \infty} \frac{2 \sin[L(k_z - k'_z)/2]}{L(k_z - k'_z)}.$$

After some simple algebra we obtain the result

$$\int_{-\infty}^{\infty} dz_n dz_m e^{i\omega|z_n - z_m|/c - ik_z z_n + ik'_z z_m} = \lim_{L \rightarrow \infty} L^2 \left\{ 1 - \frac{2i\omega/c}{L[k_z^2 - (\omega/c)^2]} \right\} \delta_{k_z k'_z}. \quad (117)$$

In view of Eqs. (116) and (117), the function (115) takes the form

$$g_f^{(\pm)}(\mathbf{k}, \mathbf{k}', \omega) = \pm \frac{i\omega d_z^f \sqrt{\pi S_0 \hbar \omega \operatorname{Re} \sigma_{zz}(\omega)}}{(2\pi)^2 c \sigma_{zz}(\omega) R_{CN}} \lim_{L \rightarrow \infty} \left\{ 1 - \frac{2i\omega/c}{L[k_z^2 - (\omega/c)^2]} \right\} \delta_{\mathbf{k}\mathbf{k}'}. \quad (118)$$

We have taken into account here that $\delta_{k_\varphi k'_\varphi} \delta_{k_z k'_z} = \delta_{\mathbf{k}\mathbf{k}'}$, as well as the fact that $(R_{CN} L / NS_0)^2 = 1/(2\pi)^2$. This can be further simplified by noticing that only absolute value squared of the interaction matrix element matters in calculations of observables. We then have

$$\left| 1 - \frac{2i\omega/c}{L[k_z^2 - (\omega/c)^2]} \right|^2 = 1 + \frac{\alpha}{u^2} \approx 1 + \frac{\alpha}{u^2 + \alpha^2}$$

with $u = (ck_z/\omega)^2 - 1$, and $\alpha = (2c/L\omega)^2$ being the small parameter which tends to zero as $L \rightarrow \infty$. Using further the formula (see, e.g., Ref. [74])

$$\delta(u) = \frac{1}{\pi} \lim_{\alpha \rightarrow 0} \frac{\alpha}{u^2 + \alpha^2},$$

and the basic properties of the δ -function, we arrive at

$$\lim_{L \rightarrow \infty} \left| 1 - \frac{2i\omega/c}{L[k_z^2 - (\omega/c)^2]} \right|^2 = 1 + \frac{\pi c |k_z|}{2} [\delta(\omega + ck_z) + \delta(\omega - ck_z)] \quad (119)$$

We also have

$$\left| \frac{\sqrt{\operatorname{Re} \sigma_{zz}(\omega)}}{\sigma_{zz}(\omega)} \right|^2 = \operatorname{Re} \frac{1}{\sigma_{zz}(\omega)}. \quad (120)$$

Equation (118), in view of Eqs. (119) and (120), is rewritten effectively as follows

$$g_f^{(\pm)}(\mathbf{k}, \mathbf{k}', \omega) = \pm i D_f(\omega) \delta_{\mathbf{k}\mathbf{k}'} \quad (121)$$

with

$$D_f(\omega) = \frac{\omega d_z^f \sqrt{\pi S_0 \hbar \omega \operatorname{Re}[1/\sigma_{zz}(\omega)]}}{(2\pi)^2 c R_{CN}} \sqrt{1 + \frac{\pi c |k_z|}{2} [\delta(\omega + ck_z) + \delta(\omega - ck_z)]}. \quad (122)$$

In terms of the simplified interaction matrix element (121), the \mathbf{k} -representation of the Hamiltonian (1)–(13) takes the following (symmetrized) form

$$\hat{H} = \frac{1}{2} \sum_{\mathbf{k}} \hat{H}_{\mathbf{k}}, \quad (123)$$

where

$$\begin{aligned} \hat{H}_{\mathbf{k}} = & \sum_f E_f(\mathbf{k}) \left(B_{\mathbf{k},f}^\dagger B_{\mathbf{k},f} + B_{-\mathbf{k},f}^\dagger B_{-\mathbf{k},f} \right) \\ & + \int_0^\infty d\omega \hbar \omega \left[\hat{f}^\dagger(\mathbf{k}, \omega) \hat{f}(\mathbf{k}, \omega) + \hat{f}^\dagger(-\mathbf{k}, \omega) \hat{f}(-\mathbf{k}, \omega) \right] \\ & + \sum_f \int_0^\infty d\omega i D_f(\omega) \left(B_{\mathbf{k},f}^\dagger + B_{-\mathbf{k},f} \right) \left[\hat{f}(\mathbf{k}, \omega) - \hat{f}^\dagger(-\mathbf{k}, \omega) \right] + h.c. \end{aligned} \quad (124)$$

with $D_f(\omega)$ given by Eq. (122). To diagonalize this Hamiltonian, we follow Bogoliubov's canonical transformation technique (see, e.g., Ref. [74]). The canonical transformation of the exciton and photon operators is of the form

$$B_{\mathbf{k},f} = \sum_{\mu=1,2} \left[u_\mu(\mathbf{k}, \omega_f) \hat{\xi}_\mu(\mathbf{k}) + v_\mu(\mathbf{k}, \omega_f) \hat{\xi}_\mu^\dagger(-\mathbf{k}) \right], \quad (125)$$

$$\hat{f}(\mathbf{k}, \omega) = \sum_{\mu=1,2} \left[u_\mu^*(\mathbf{k}, \omega) \hat{\xi}_\mu(\mathbf{k}) + v_\mu^*(\mathbf{k}, \omega) \hat{\xi}_\mu^\dagger(-\mathbf{k}) \right], \quad (126)$$

where the new operators, $\hat{\xi}_\mu(\mathbf{k})$ and $\hat{\xi}_\mu^\dagger(\mathbf{k}) = [\hat{\xi}_\mu(\mathbf{k})]^\dagger$, annihilate and create, respectively, the coupled exciton-photon excitations of branch μ on the nanotube surface. They satisfy the bosonic commutation relations of the form

$$\left[\hat{\xi}_\mu(\mathbf{k}), \hat{\xi}_{\mu'}^\dagger(\mathbf{k}') \right] = \delta_{\mu\mu'} \delta_{\mathbf{k}\mathbf{k}'}, \quad (127)$$

which, along with the reversibility requirement of Eqs. (125) and (126), impose the

following constraints on the transformation functions u_μ and v_μ

$$\begin{aligned} & \sum_f [u_\mu^*(\mathbf{k}, \omega_f) u_{\mu'}(\mathbf{k}, \omega_f) - v_\mu(\mathbf{k}, \omega_f) v_{\mu'}^*(\mathbf{k}, \omega_f)] \\ & + \int_0^\infty d\omega [u_\mu(\mathbf{k}, \omega) u_{\mu'}^*(\mathbf{k}, \omega) - v_\mu^*(\mathbf{k}, \omega) v_{\mu'}(\mathbf{k}, \omega)] = \delta_{\mu\mu'}, \\ & \sum_\mu [u_\mu^*(\mathbf{k}, \omega_f) u_\mu(\mathbf{k}, \omega_{f'}) - v_\mu^*(\mathbf{k}, \omega_f) v_\mu(\mathbf{k}, \omega_{f'})] = \delta_{ff'}, \\ & \sum_\mu [u_\mu^*(\mathbf{k}, \omega) u_\mu(\mathbf{k}, \omega') - v_\mu^*(\mathbf{k}, \omega) v_\mu(\mathbf{k}, \omega')] = \delta(\omega - \omega'). \end{aligned}$$

Here, the first equation guarantees the fulfilment of the commutation relations (127), whereas the second and the third ensure that Eqs. (125) and (126) are inverted to yield $\hat{\xi}_\mu(\mathbf{k})$ as given by Eq. (15). Other possible combinations of the transformation functions are identically equal to zero.

The proper transformation functions that diagonalize the Hamiltonian (124) to bring it to the form (14), are determined by the identity

$$\hbar\omega_\mu(\mathbf{k}) \hat{\xi}_\mu(\mathbf{k}) = [\hat{\xi}_\mu(\mathbf{k}), \hat{H}_\mathbf{k}]. \quad (128)$$

Putting Eqs. (15) and (124) into Eq. (128) and using the bosonic commutation relations for the exciton and photon operators on the right, one obtains (\mathbf{k} -argument is omitted for brevity)

$$\begin{aligned} (\hbar\omega_\mu - E_f) u_\mu^*(\omega_f) &= -i \int_0^\infty d\omega D_f(\omega) [u_\mu(\omega) - v_\mu^*(\omega)], \\ (\hbar\omega_\mu + E_f) v_\mu(\omega_f) &= i \int_0^\infty d\omega D_f(\omega) [u_\mu(\omega) - v_\mu^*(\omega)], \\ \hbar(\omega_\mu - \omega) u_\mu(\omega) &= i \sum_f D_f(\omega) [u_\mu^*(\omega_f) + v_\mu(\omega_f)], \\ \hbar(\omega_\mu + \omega) v_\mu^*(\omega) &= i \sum_f D_f(\omega) [u_\mu^*(\omega_f) + v_\mu(\omega_f)]. \end{aligned}$$

These simultaneous equations define the complex transformation functions u_μ and v_μ uniquely. They also define the dispersion relation (the energies $\hbar\omega_\mu$, $\mu = 1, 2$) of the coupled exciton-photon (or exciton-plasmon, to be exact) excitations on the nanotube surface. Substituting u_μ and v_μ^* from the third and fourth equations into the first one, one has

$$\left[\hbar\omega_\mu - E_f - \frac{4E_f}{\hbar\omega_\mu + E_f} \int_0^\infty d\omega \frac{\omega |D_f(\omega)|^2}{\hbar(\omega_\mu^2 - \omega^2)} \right] u_\mu^*(\omega_f) = 0,$$

whereby, since the functions u_μ^* are non-zero, the dispersion relation we are interested in becomes

$$(\hbar\omega_\mu)^2 - E_f^2 - 4E_f \int_0^\infty d\omega \frac{\omega |D_f(\omega)|^2}{\hbar(\omega_\mu^2 - \omega^2)} = 0. \quad (129)$$

The energy E_0 of the ground state of the coupled exciton-plasmon excitations is found by plugging Eq. (15) into Eq. (14) and comparing the result with Eqs. (123) and (124). This yields

$$E_0 = - \sum_{\mathbf{k}, \mu=1,2} \hbar\omega_\mu(\mathbf{k}) \left[\sum_f |v_\mu(\mathbf{k}, \omega_f)|^2 + \int_0^\infty d\omega |v_\mu(\mathbf{k}, \omega)|^2 \right].$$

Using further $D_f(\omega)$ as explicitly given by Eq. (122), the dispersion relation (129) is rewritten as follows

$$(\hbar\omega_\mu)^2 - E_f^2 = \frac{E_f S_0 |d_z^f|^2}{4\pi^3 c^2 R_{CN}^2} \left\{ \int_0^\infty d\omega \frac{\omega^4 \text{Re}[1/\sigma_{zz}(\omega)]}{\omega_\mu^2 - \omega^2} + \frac{\pi(c|k_z|)^5 \text{Re}[1/\sigma_{zz}(c|k_z|)]}{\omega_\mu^2 - (c|k_z|)^2} \right\}.$$

Here we have taken into account the general property $\sigma_{zz}(\omega) = \sigma_{zz}^*(-\omega)$, which originates from the time-reversal symmetry requirement, in the second term on the right hand side. This term comes from the two delta functions in $|D_f(\omega)|^2$, and describes the contribution of the spatial dispersion (wave-vector dependence) to the formation of the exciton-plasmons. We neglect this term in what follows because the spatial dispersion is neglected in the nanotube's axial surface conductivity in our model, and, secondly, because it is seen to be very small for not too large excitonic wave vectors. Thus, converting to the dimensionless variables (17), we arrive at the dispersion relation (16) with the exciton spontaneous decay (recombination) rate and the plasmon DOS given by Eqs. (18) and (19), respectively.

Lastly, bearing in mind that the delta functions in $|D_f(\omega)|^2$ are responsible for the spatial dispersion which we neglect in our model, and therefore dropping them out from the squared interaction matrix element (121), we arrive at the property (45).

Appendix D

Effective longitudinal potential in the presence of the perpendicular electrostatic field

Here we analyze the set of equations (27)–(29), and show that the attractive cusptype cutoff potential (32) with the field dependent cutoff parameter (33) is a uniformly valid approximation for the effective electron-hole Coulomb interaction potential (30) in the exciton binding energy equation (29).

We rewrite Eqs. (27) and (28) in the form of a single equation as follows

$$\left(\frac{d^2}{d\varphi^2} + q^2 + p \cos \varphi \right) \psi(\varphi) = 0. \quad (130)$$

Here, $\varphi = \varphi_{e,h}$, $\psi = \psi_{e,h}$, $q = R_{CN} \sqrt{2m_{e,h}\varepsilon_{e,h}/\hbar}$, and $p = \pm 2em_{e,h}R_{CN}^3F/\hbar^2$ with the (+)-sign to be taken for the electron and the (-)-sign to be taken for the hole. We are interested in the solutions to Eq. (130) which satisfy the 2π -periodicity condition $\psi(\varphi) = \psi(\varphi + 2\pi)$. The change of variable $\varphi = 2t$ transfers this equation to the well known Mathieu's equation (see, e.g., Refs. [119, 114]), reducing the solution's period by the factor of two. The exact solutions of interest are, therefore, given by the odd Mathieu functions $se_{2m+2}(t = \varphi/2)$ with the eigen values b_{2m+2} , where m is a nonnegative integer (notations of Ref. [119]). These are the solutions to the Sturm-Liouville problem with boundary conditions on functions, not on their derivatives.

It is easier to estimate the z -dependence of the potential (30) if the functions $\psi_{e,h}(\varphi_{e,h})$ are known explicitly. So, we do solve Eq. (130) using the second order perturbation theory in the external field (the term $p \cos \varphi$). The second order field corrections are also of practical importance in the most of experimental applications.

The unperturbed problem yields the two linearly independent normalized eigen functions and the eigen values as follows

$$\psi_j^{(0)}(\varphi) = \frac{\exp(\pm ij\varphi)}{\sqrt{2\pi}}, \quad q = j = \frac{R_{CN}}{\hbar} \sqrt{2m_{e,h}\varepsilon_{e,h}^{(0)}} \quad (131)$$

with j being a nonnegative integer. The energies $\varepsilon_{e,h}^{(0)}(j)$ are doubly degenerate with the exception of $\varepsilon_{e,h}^{(0)}(0) = 0$, which we will discard since it results in the zero unperturbed band gap according to Eq. (8). The perturbation $p \cos \varphi$ does not lift the degeneracy of the unperturbed states. Therefore, we use the standard nondegenerate perturbation theory with the basis wave functions set above (plus sign selected for definiteness) to calculate the energies and the wave functions to the second order in perturbation. The standard procedure (see, e.g., Ref. [95]) yields

$$\begin{aligned} \psi_{j e,h}(\varphi_{e,h}) = & \left(1 - \left\{ \frac{\vartheta(j-2)}{[(j-1)^2 - j^2]^2} + \frac{1}{[(j+1)^2 - j^2]^2} \right\} \frac{m_{e,h}^2 e^2 R_{CN}^6 F^2}{2\hbar^4} \right) \psi_{j e,h}^{(0)}(\varphi_{e,h}) \\ & \pm \left[\frac{\vartheta(j-2)\psi_{j-1 e,h}^{(0)}(\varphi_{e,h})}{(j-1)^2 - j^2} + \frac{\psi_{j+1 e,h}^{(0)}(\varphi_{e,h})}{(j+1)^2 - j^2} \right] \frac{m_{e,h} e R_{CN}^3 F}{\hbar^2} \\ & + \left\{ \frac{\vartheta(j-2)\vartheta(j-3)\psi_{j-2 e,h}^{(0)}(\varphi_{e,h})}{[(j-1)^2 - j^2][(j-2)^2 - j^2]} + \frac{\psi_{j+2 e,h}^{(0)}(\varphi_{e,h})}{[(j+1)^2 - j^2][(j+2)^2 - j^2]} \right\} \frac{m_{e,h}^2 e^2 R_{CN}^6 F^2}{\hbar^4}. \end{aligned} \quad (132)$$

Here, j is a positive integer, and the theta-functions ensure that $j = 1$ is the ground state of the system. The corresponding energies are as follows

$$\varepsilon_{e,h} = \frac{\hbar^2 j^2}{2m_{e,h} R_{CN}^2} - \frac{m_{e,h} e^2 R_{CN}^4 w_j}{2\hbar^2} F^2 \quad (133)$$

with w_j given by Eq. (34), thus, according to Eq. (8), resulting in the nanotube's band gap as given by Eq. (37).

From Eq. (132), in view of Eq. (131), we have the following to the second order in the field

$$\begin{aligned} |\psi_e(\varphi_e)|^2 |\psi_h(\varphi_h)|^2 \approx & \frac{1}{4\pi^2} \left[1 - 2(m_h \cos \varphi_h - m_e \cos \varphi_e) \frac{e R_{CN}^3 w_j}{\hbar^2} F \right. \\ & \left. + 2(m_h^2 \cos 2\varphi_h + m_e^2 \cos 2\varphi_e) \frac{e^2 R_{CN}^6 v_j}{\hbar^4} F^2 - 4\mu M_{ex} \cos \varphi_e \cos \varphi_h \frac{e^2 R_{CN}^6 w_j^2}{\hbar^4} F^2 \right], \end{aligned} \quad (134)$$

where

$$v_j = \frac{\vartheta(j-2)}{(j-1)^2 - j^2} \left\{ \frac{\vartheta(j-3)}{(j-2)^2 - j^2} + \frac{1}{(j+1)^2 - j^2} \right\} + \frac{1}{[(j+1)^2 - j^2][(j+2)^2 - j^2]}.$$

Plugging Eqs. (134) and (31) into Eq. (30) and noticing that the integrals involving linear combinations of the cosine-functions are strongly suppressed due to the integration over the cosine period, and are therefore negligible compared to the one involving the quadratic cosine-combination, we obtain

$$V_{\text{eff}}(z) = -\frac{e^2}{4\pi^2 \epsilon} \int_0^{2\pi} d\varphi_e \int_0^{2\pi} d\varphi_h \frac{1 - 2 \cos \varphi_e \cos \varphi_h \Delta_j(F)}{\{z^2 + 4R_{CN}^2 \sin^2[(\varphi_e - \varphi_h)/2]\}^{1/2}} \quad (135)$$

with $\Delta_j(F)$ given by Eq. (34).

The next step is to perform the double integration in Eq. (135). We have to evaluate the two double integrals. They are

$$I_1 = \int_0^{2\pi} d\varphi_e \int_0^{2\pi} \frac{d\varphi_h}{\{z^2 + 4R_{CN}^2 \sin^2[(\varphi_e - \varphi_h)/2]\}^{1/2}} \quad (136)$$

and

$$I_2 = \int_0^{2\pi} d\varphi_e \int_0^{2\pi} \frac{d\varphi_h \cos \varphi_e \cos \varphi_h}{\{z^2 + 4R_{CN}^2 \sin^2[(\varphi_e - \varphi_h)/2]\}^{1/2}}. \quad (137)$$

We first notice that both I_1 and I_2 can be equivalently rewritten as follows

$$\int_0^{2\pi} d\varphi_e \int_0^{2\pi} d\varphi_h \dots = 2 \int_0^{2\pi} d\varphi_e \int_0^{\varphi_e} d\varphi_h \dots \quad (138)$$

due to the symmetry of the integrands with respect to the $(\varphi_e = \varphi_h)$ -line. Using this property, we substitute φ_h with the new variable $t = \sin[(\varphi_e - \varphi_h)/2]$ in Eqs. (136) and (137). This, after simplifications, yields

$$I_1 = 4 \int_0^{2\pi} d\varphi_e \int_0^{\sin(\varphi_e/2)} \frac{dt}{[(1-t^2)(z^2 + 4R_{CN}^2 t^2)]^{1/2}} \quad (139)$$

and

$$I_2 = 4 \int_0^{2\pi} d\varphi_e \cos^2 \varphi_e \int_0^{\sin(\varphi_e/2)} \frac{dt (1-2t^2)}{[(1-t^2)(z^2 + 4R_{CN}^2 t^2)]^{1/2}}. \quad (140)$$

Here, the inner integrals are reduced to the incomplete elliptical integrals of the first and second kinds (see, e.g., Ref. [114]).

We continue the evaluation of Eqs. (139) and (140) by expanding the denominators of the integrands in series at large and small $|z|$ as compared to the CN diameter $2R_{CN}$. One has

$$\frac{1}{(z^2 + 4R_{CN}^2 t^2)^{1/2}} \approx \frac{1}{|z|} \left[1 - \frac{1}{2} \left(\frac{2R_{CN}t}{|z|} \right)^2 + \frac{3}{8} \left(\frac{2R_{CN}t}{|z|} \right)^4 - \frac{5}{16} \left(\frac{2R_{CN}t}{|z|} \right)^6 + \dots \right]$$

for $|z|/2R_{CN} \gg 1$, and

$$\int_0^{\sin(\varphi_e/2)} \frac{dt f(t)}{[(1-t^2)(z^2 + 4R_{CN}^2 t^2)]^{1/2}} = \frac{1}{2R_{CN}} \lim_{(|z|/2R_{CN}) \rightarrow 0} \int_{|z|/2R_{CN}}^{\sin(\varphi_e/2)} \frac{f(t) dt}{t\sqrt{1-t^2}}$$

for $|z|/2R_{CN} \ll 1$ [$f(t)$ is a polynomial function]. Using these in Eqs. (139) and (140), we arrive at

$$I_1 \approx \begin{cases} \frac{4\pi}{R_{CN}} \left[\ln \left(\frac{4R_{CN}}{|z|} \right) - \frac{1}{4} \left(\frac{|z|}{2R_{CN}} \right)^2 \right], & \frac{|z|}{2R_{CN}} \ll 1 \\ \frac{4\pi^2}{|z|} \left[1 - \frac{1}{4} \left(\frac{2R_{CN}}{|z|} \right)^2 + \frac{9}{64} \left(\frac{2R_{CN}}{|z|} \right)^4 \right], & \frac{|z|}{2R_{CN}} \gg 1 \end{cases}$$

and

$$I_2 \approx \begin{cases} \frac{4\pi}{R_{CN}} \left[\frac{1}{2} \ln \left(\frac{4R_{CN}}{|z|} \right) - 1 + \frac{3}{8} \left(\frac{|z|}{2R_{CN}} \right)^2 \right], & \frac{|z|}{2R_{CN}} \ll 1 \\ \frac{\pi^2}{4|z|} \left(\frac{2R_{CN}}{|z|} \right)^2 \left[1 - \frac{3}{4} \left(\frac{2R_{CN}}{|z|} \right)^2 \right], & \frac{|z|}{2R_{CN}} \gg 1 \end{cases}$$

Plugging these I_1 and I_2 into Eq. (135) and retaining only leading expansion terms yields

$$V_{\text{eff}}(z) \approx \begin{cases} -\frac{e^2 [1 - \Delta_j(F)]}{\pi \epsilon R_{CN}} \ln \left(\frac{4R_{CN}}{|z|} \right), & \frac{|z|}{2R_{CN}} \ll 1 \\ -\frac{e^2}{\epsilon |z|}, & \frac{|z|}{2R_{CN}} \gg 1 \end{cases} \quad (141)$$

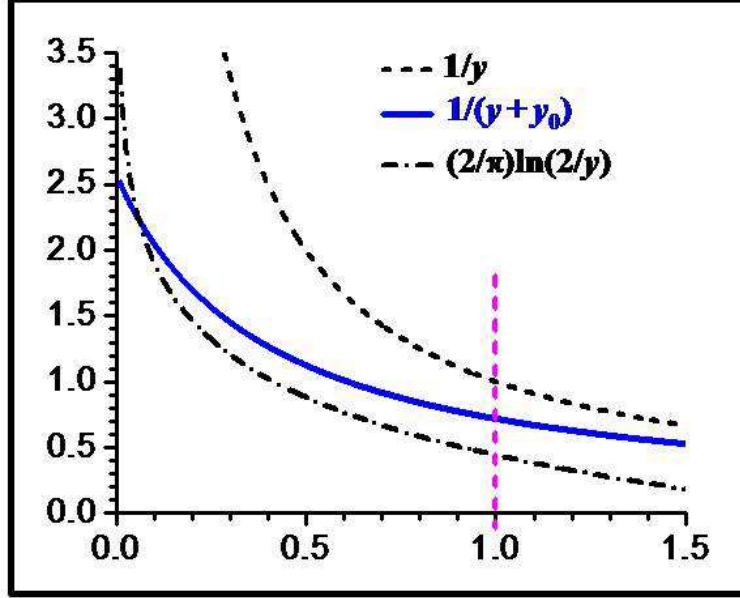


Figure 14: The dimensionless function (142) with the zero-field cutoff parameter (143). See text for details.

We see from Eq. (141) that, to the leading order in the series expansion parameter, the perpendicular electrostatic field does not affect the longitudinal electron-hole Coulomb potential at large distances $|z| \gg 2R_{CN}$, as one would expect. At short distances $|z| \ll 2R_{CN}$ the situation is different, however. The potential decreases logarithmically with the field dependent amplitude as $|z|$ goes down. The amplitude of the potential decreases quadratically as the field increases [see Eq. (34)], thereby slowing down the potential fall-off with decreasing $|z|$, or, in other words, making the potential shallower as the field increases. Such a behavior can be uniformly approximated for all $|z|$ by an appropriately chosen attractive cusp-type cutoff potential with the field dependent cutoff parameter. Indeed, consider the dimensionless function $f(y) = -2R_{CN}\epsilon V_{\text{eff}}/e^2$ of the dimensionless variable $y = |z|/2R_{CN}$. Then, according to Eq. (141), one has

$$f(y) = \begin{cases} \Phi_1(y) = \frac{2}{\pi} [1 - \Delta_j(F)] \ln\left(\frac{2}{y}\right), & 0 < y \ll 1 \\ \Phi_2(y) = \frac{1}{y}, & y \gg 1 \end{cases}$$

Now introduce the function

$$\Phi(y) = \frac{1}{y + y_0} \quad (142)$$

with the cutoff parameter y_0 selected in such a way as to satisfy the condition

$\Phi(1) = [\Phi_1(1) + \Phi_2(1)]/2$. This yields

$$y_0 = \frac{\pi - 2 \ln 2 [1 - \Delta_j(F)]}{\pi + 2 \ln 2 [1 - \Delta_j(F)]}. \quad (143)$$

Figure 14 shows the zero-field behavior of the $\Phi(y)$ function as compared to the corresponding $\Phi_1(y)$ and $\Phi_2(y)$ functions. We see that $\Phi(y)$ gradually approaches $\Phi_2(y) = 1/y$ for increasing $y > 1$. For decreasing $y < 1$, on the other hand, $\Phi(y)$ is very close to the logarithmic behavior as given by $\Phi_1(y)$, with the exception that there is no divergence at $y \sim 0$ due to the presence of the cutoff. The cutoff parameter (143) is field dependent, decreasing as the field grows, which is consistent with the behavior of the original potential (141). Multiplying Eq. (142) by the dimensional factor $-e^2/2R_{CN}\epsilon$ and putting $y = |z|/2R_{CN}$, we obtain the attractive longitudinal cusp-type cutoff potential (32) we build our analysis on in this paper.

References

- [1] R.Saito, G.Dresselhaus, and M.S.Dresselhaus, *Science of Fullerenes and Carbon Nanotubes* (Imperial College Press, London, 1998).
- [2] H.Dai, Surf. Sci. **500**, 218 (2002).
- [3] L.X.Zheng, M.J.O'Connell, S.K.Doorn, X.Z.Liao, Y.H. Zhao, E.A.Akhadov, M.A.Hoffbauer, B.J.Roop, Q.X.Jia, R.C.Dye, D.E.Peterson, S.M.Huang, J.Liu and Y.T.Zhu, Nature Materials **3**, 673 (2004).
- [4] S.M.Huang, B.Maynor, X.Y.Cai, and J.Liu, Advanced Materials **15**, 1651 (2003).
- [5] R.H.Baughman, A.A.Zakhidov, and W.A.de Heer, Science **297**, 787 (2002).
- [6] A.Popescu, L.M.Woods, and I.V.Bondarev, Nanotechnology **19**, 435702 (2008).
- [7] J.E.Trancik, S.C.Barton, and J.Hone, Nano Lett. **8**, 982 (2008).
- [8] I.V.Bondarev, J. Comput. Theor. Nanosci. **7**, 1673 (2010) (invited review article for the special issue on "Technology Trends and Theory of Nanoscale Devices for Quantum Applications", American Scientific Publishers, USA).
- [9] I.V.Bondarev and Ph.Lambin, in: *Trends in Nanotubes Research* (Nova Science, NY, 2006). Ch.6, pp.139-183.
- [10] I.V.Bondarev and B.Vlahovic, Phys. Rev. B **74**, 073401 (2006).
- [11] I.V.Bondarev and B.Vlahovic, Phys. Rev. B **75**, 033402 (2007).
- [12] I.V.Bondarev, J. Electron. Mater. **36**, 1579(2007).
- [13] I.V.Bondarev, Optics & Spectroscopy (Springer) **103**, 366 (2007).
- [14] H.Shimoda, B.Gao, X.P.Tang, A.Kleinhammes, L.Fleming, Y.Wu, and O.Zhou, Phys. Rev. Lett. **88**, 015502 (2001).
- [15] G.-H. Jeong, A.A.Farajian, R.Hatakeyama, T.Hirata, T.Yaguchi, K.Tohji, H.Mizuseki, and Y.Kawazoe, Phys. Rev. B **68**, 075410 (2003)
- [16] G.-H.Jeong, A.A.Farajian, T.Hirata, R.Hatakeyama, K. Tohji, T.M.Briere, H.Mizuseki, and Y.Kawazoe, Thin Solid Films **435**, 307 (2003).
- [17] M.Khazaei, A.A.Farajian, G.-H.Jeong, H.Mizuseki, T. Hirata, R.Hatakeyama, and Y.Kawazoe, J. Phys. Chem. B **108**, 15529 (2004).
- [18] A.Högele, Ch.Galland, M.Winger, and A.Imamoğlu, Phys. Rev. Lett. **100**, 217401 (2008).

- [19] T.G.Pedersen, Phys. Rev. B **67**, 073401 (2003).
- [20] T.G.Pedersen, Carbon **42**, 1007 (2004).
- [21] R.B.Capaz, C.D.Spataru, S.Ismail-Beigi, and S.G.Louie, Phys. Rev. B **74**, 121401(R) (2006).
- [22] C.D.Spataru, S.Ismail-Beigi, L.X.Benedict, and S.G. Louie, Phys. Rev. Lett. **92**, 077402 (2004).
- [23] F.Wang, G.Dukovic, L.E.Brus, and T.F.Heinz, Phys. Rev. Lett. **92**, 177401 (2004).
- [24] F.Wang, G.Dukovic, L.E.Brus, and T.F.Heinz, Science **308**, 838 (2005).
- [25] A.Hagen, M.Steiner, M.B.Raschke, C.Lienau, T.Hertel, H.Qian, A.J.Meixner, and A.Hartschuh, Phys. Rev. Lett. **95**, 197401 (2005).
- [26] F.Plentz, H.B.Ribeiro, A.Jorio, M.S.Strano, M.A.Pimenta, Phys. Rev. Lett. **95**, 247401 (2005).
- [27] F.Xia, M.Steiner, Y.-M.Lin, and Ph.Avouris, Nature Nanotechnology **3**, 609 (2008).
- [28] B.F.Habenicht and O.V.Prezhdo, Phys. Rev. Lett. **100**, 197402 (2008).
- [29] V.Perebeinos, J.Tersoff, and Ph.Avouris, Phys. Rev. Lett. **94**, 027402 (2005).
- [30] M.Lazzeri, S.Piscanec, F.Mauri, A.C.Ferrari, and J.Robertson, Phys. Rev. Lett. **95**, 236802 (2005).
- [31] S.Piscanec, M.Lazzeri, J.Robertson, A.C.Ferrari, and F. Mauri, Phys. Rev. B **75**, 035427 (2007).
- [32] T.G.Pedersen, K.Pedersen, H.D.Cornean, and P.Duclos, NanoLett. **5**, 291 (2005).
- [33] D.J.Styers-Barnett, S.P.Ellison, B.P.Mehl, B.C.Westlake, R.L.House, C.Park, K.E.Wise, and J.M.Papanikolas, J. Phys. Chem. C **112**, 4507 (2008).
- [34] I.V.Bondarev, H.Qasmi, Physica E **40**, 2365 (2008).
- [35] I.V.Bondarev, K.Tatur, and L.M.Woods, Optics Commun. **282**, 661 (2009).
- [36] I.V.Bondarev, K.Tatur, and L.M.Woods, Optics and Spectroscopy **108**, 376 (2010).
- [37] I.V.Bondarev, L.M.Woods, and K.Tatur, Phys. Rev. B **80**, 085407 (2009).

- [38] S.Zaric, G.N.Ostojic, J.Shaver, J.Kono, O.Portugall, P.H.Frings, G.L.J.A.Rikken, M.Furis, S.A.Crooker, X. Wei, V.C.Moore, R.H.Hauge, and R.E.Smalley, *Phys. Rev. Lett.* **96**, 016406 (2006).
- [39] A.Srivastava, H.Htoon, V.I.Klimov, and J.Kono, *Phys. Rev. Lett.* **101**, 087402 (2008).
- [40] V.Perebeinos and Ph.Avouris, *Nano Lett.* **7**, 609 (2007).
- [41] M.S.Dresselhaus, G.Dresselhaus, R.Saito, and A.Jorio, *Annu. Rev. Phys. Chem.* **58**, 719 (2007).
- [42] A.Goodsell, T.Ristroph, J.A.Golovchenko, and L.V.Hau, *Phys. Rev. Lett.* **104**, 133002 (2010).
- [43] H.Qian, C.Georgi, N.Anderson, A.A.Green, M.C.Hersam, L.Novotny, and A.Hartschuh, *Nano Lett.* **8**, 1363 (2008).
- [44] P.H.Tan, A.G.Rozhin, T.Hasan, P.Hu, V.Scardaci, W.I.Milne, and A.C.Ferrari, *Phys. Rev. Lett.* **99**, 137402 (2007).
- [45] R.Fermani, S.Scheel, and P.L.Knight, *Phys. Rev. A* **75**, 062905 (2007).
- [46] A.Popescu and L.M.Woods, *Appl. Phys. Lett.* **95**, 203507 (2009).
- [47] W.Vogel and D.-G.Welsch, *Quantum Optics* (Wiley-VCH, NY, 2006). Ch.10, p.337.
- [48] L.Knöll, S.Scheel, and D.-G.Welsch, in: *Coherence and Statistics of Photons and Atoms*, edited by J.Peřina (Wiley, NY, 2001).
- [49] S.Y.Buhmann and D.-G.Welsch, *Prog. Quantum Electron.* **31**, 51 (2007).
- [50] T.Pichler, M.Knupfer, M.S.Golden, J.Fink, A.Rinzler, and R.E.Smalley, *Phys. Rev. Lett.* **80**, 4729 (1998).
- [51] C.D.Spataru, S.Ismail-Beigi, R.B.Capaz, and S.G.Louie, *Phys. Rev. Lett.* **95**, 247402 (2005).
- [52] Y.-Z.Ma, C.D.Spataru, L.Valkunas, S.G.Louie, and G.R. Fleming, *Phys. Rev. B* **74**, 085402 (2006).
- [53] J.Bellessa, C.Bonnand, J.C.Plenet, and J.Mugnier, *Phys. Rev. Lett.* **93**, 036404 (2004).
- [54] W.Zhang, A.O.Govorov, and G.W.Bryant, *Phys. Rev. Lett.* **97**, 146804 (2006).
- [55] Y.Fedutik, V.V.Temnov, O.Schöps, U.Woggon, and M.V. Artemyev, *Phys. Rev. Lett.* **99**, 136802 (2007).

- [56] G.L.Klimchitskaya, U.Mohideen, and V.M.Mostepepanenko, *Rev. Mod. Phys.* **81**, 1827 (2009).
- [57] H.B.Chan, V.A.Aksyuk, R.N.Kleiman, D.J.Bishop, and F.Capasso, *Phys. Rev. Lett.* **87**, 211801 (2001); *Science* **291**, 1941 (2001).
- [58] I.V.Bondarev, G.Ya.Slepyan and S.A.Maksimenko, *Phys. Rev. Lett.* **89**, 115504 (2002).
- [59] I.V.Bondarev and Ph.Lambin, *Phys. Rev. B* **70**, 035407 (2004).
- [60] I.V.Bondarev and Ph.Lambin, *Phys. Lett. A* **328**, 235 (2004).
- [61] I.V.Bondarev and Ph.Lambin, *Solid State Commun.* **132**, 203 (2004).
- [62] I.V.Bondarev and Ph.Lambin, *Phys. Rev. B* **72**, 035451 (2005).
- [63] L.X.Benedict, S.G.Louie, and M.L.Cohen, *Phys. Rev. B* **52**, 8541 (1995).
- [64] S.Tasaki, K.Maekawa, and T.Yamabe, *Phys. Rev. B* **57**, 9301 (1998).
- [65] Z.M.Li, Z.K.Tang, H.J.Liu, N.Wang, C.T.Chan, R.Saito, S.Okada, G.D.Li, J.S.Chen, N.Nagasawa, and S.Tsuda, *Phys. Rev. Lett.* **87**, 127401 (2001).
- [66] A.G.Marinopoulos, L.Reining, A.Rubio, and N.Vast, *Phys. Rev. Lett.* **91**, 046402 (2003).
- [67] T.Ando, *J. Phys. Soc. Jpn.* **74**, 777 (2005).
- [68] B.Kozinsky and N.Marzari, *Phys. Rev. Lett.* **96**, 166801 (2006).
- [69] H.Haken, *Quantum Field Theory of Solids*, (North-Holland, Amsterdam, 1976).
- [70] S.Uryu and T.Ando, *Phys. Rev. B* **74**, 155411 (2006).
- [71] L.D.Landau and E.M.Lifshits, *The Classical Theory of Fields* (Pergamon, New York, 1975).
- [72] K.Kempa and P.R.Chura, special edition of the Kluwer Academic Press Journal, edited by L.Liz-Marzan and M.Giersig (2002).
- [73] K.Kempa, D.A.Broido, C.Beckwith, and J.Cen, *Phys. Rev. B* **40**, 8385 (1989).
- [74] A.S.Davydov, *Quantum Mechanics* (Pergamon, New York, 1976).
- [75] V.N.Popov, L.Henrard, *Phys. Rev. B* **70**, 115407 (2004).
- [76] M.F.Lin, D.S.Chuu, and K.W.-K.Shung, *Phys. Rev. B* **56**, 1430 (1997).
- [77] H.Ehrenreich and M.H.Cohen, *Phys. Rev.* **115**, 786 (1959).

- [78] X.Blase, L.X.Benedict, E.L.Shirley, and S.G.Louie, Phys. Rev. Lett. **72**, 1878 (1994).
- [79] K.Kempa, Phys. Rev. B **66**, 195406 (2002).
- [80] E.Hanamura, Phys. Rev. B **38**, 1228 (1988).
- [81] J.P.Reithmaier, G.Şek, A.Löffler, C.Hofmann, S.Kuhn, S.Reitzenstein, L.V.Keldysh, V.D.Kulakovskii, T.L.Reinecke, and A.Forchel, Nature **432**, 197 (2004).
- [82] T.Yoshie, A.Scherer, J.Hendrickson, G.Khitrova, H.M. Gibbs, G.Rupper, C.Ell, O.B.Shchekin, and D.G.Deppe, Nature **432**, 200 (2004).
- [83] E.Peter, P.Senellart, D.Martrou, A.Lemaître, J.Hours, J.M.Gérard, and J.Bloch, Phys. Rev. Lett. **95**, 067401 (2005).
- [84] D.A.B.Miller, D.S.Chemla, T.C.Damen, A.C.Gossard, W.Wiegmann, T.H.Wood, and C.A.Burrus, Phys. Rev. Lett. **53**, 2173 (1984).
- [85] D.A.B.Miller, D.S.Chemla, T.C.Damen, A.C.Gossard, W.Wiegmann, T.H.Wood, and C.A.Burrus, Phys. Rev. B **32**, 1043 (1985).
- [86] A.Zrenner, E.Beham, S.Stufler, F.Findeis, M.Bichler, and G.Abstreiter, Nature **418**, 612 (2002).
- [87] H.J.Krenner, E.C.Clark, T.Nakaoka, M.Bichler, C.Scheurer, G.Abstreiter, and J.J.Finley, Phys. Rev. Lett. **97**, 076403 (2006).
- [88] T.Ando, J. Phys. Soc. Jpn. **75**, 024707 (2006).
- [89] T.Ogawa and T.Takagahara, Phys. Rev. B **44**, 8138 (1991).
- [90] A.Jorio, C.Fantini, M.A.Pimenta, R.B.Capaz, Ge.G.Samsonidze, G.Dresselhaus, M.S.Dresselhaus, J.Jiang, N. Kobayashi, A.Grüneis, and R.Saito, Phys. Rev. B **71**, 075401 (2005).
- [91] A.Suna, Phys. Rev. **135**, A111 (1964).
- [92] Y.Miyauchi, R.Saito, K.Sato, Y.Ohno, R.Iwasaki, T.Mizutani, J.Jiang, and S.Maruyama, Chem. Phys. Lett. **442**, 394 (2007).
- [93] I.V.Bondarev, Y.Nagai, M.Kakimoto, T.Hyodo, Phys. Rev. B **72**, 012303 (2005).
- [94] R.Mukamel, *Principles of Nonlinear Optical Spectroscopy* (Oxford University Press, New York, 1995).

- [95] L.D.Landau and E.M.Lifshits, *Quantum Mechanics: Non-Relativistic Theory* (Pergamon, New York, 1977).
- [96] L.P.Gor'kov and L.P.Pitaevski, Dokl. Akad. Nauk SSSR **151**, 822 (1963) [English transl.: Soviet Phys.—Dokl. **8**, 788 (1964)].
- [97] C.Herring and M.Flicker, Phys. Rev. **134**, A362 (1964); C.Herring, Rev. Mod. Phys. **34**, 631 (1962).
- [98] F.Wang, et. al., Phys. Rev. B **70**, 241403(R) (2004).
- [99] D.Abramavicius, et. al., Phys. Rev. B **79**, 195445 (2009).
- [100] A.Srivastava and J.Kono, Phys. Rev. B **79**, 205407 (2009).
- [101] M.J.Sparnaay, Physica **24**, 751 (1958).
- [102] S.K.Lamoreaux, Phys. Rev. Lett. **78**, 5 (1997).
- [103] U.Mohideen and A.Roy, Phys. Rev. Lett. **81**, 4549 (1998); F.Chen and U.Mohideen, Rev. Sci. Instrum. **72**, 3100 (2001).
- [104] J.N.Munday, F.Capasso, and V.A.Parsegian, Nature **457**, 170 (2009).
- [105] M.Bordag, U.Mohideen, and V.M.Mostepanenko, Phys. Rep. **353**, 1 (2001).
- [106] V.A.Parsegian, *van der Waals forces* (Cambridge University Press, Cityplace-Cambridge, 2005).
- [107] R.F.Rajter, R.Podgornik, V.A.Parsegian, R.H.French, and W.Y.Ching, Phys. Rev. B **76**, 045417 (2007).
- [108] A.Popescu, L.M.Woods, and I.V.Bondarev, Phys. Rev. B **77**, 115443 (2008).
- [109] M.Bordag, B.Geyer, G.L.Klimchitskaya, and V.M.Mostepanenko, Phys. Rev. B **74**, 205401 (2006).
- [110] C.T.Tai, *Dyadic Green Functions in Electromagnetic Theory*, 2nd Ed. (IEEE Press, Piscataway, NY, 1994).
- [111] L.W.Li, M.S.Leong, T.S.Yeo, and P.S.Kooi, J. Electr. Waves Appl. **14**, 961 (2000).
- [112] I.Cavero-Pelaez and K.A.Milton, Annals of Phys. **320**, 108 (2005).
- [113] K.A.Milton, L.L.DeRaad, Jr., and J.Schwinger, Ann. Phys. **115**, 388 (1978).
- [114] *Handbook of Mathematical Functions*, edited by M.Abramovitz and I.A.Stegun (Dover, New York, 1972).

- [115] N.G. van Kampen, B.R.A.Nijboer, and K.Schram, Phys. Lett. A **26**, 307 (1968).
- [116] F.Intravaia and A.Lambrecht, Phys. Rev. Lett. **94**, 110404 (2005).
- [117] J.F.Dobson, A.White, and A.Rubio, Phys. Rev. Lett. **96**, 073201 (2006).
- [118] J.D.Jackson, *Classical Electrodynamics* (Wiley, New York, 1975).
- [119] *Higher Transcendental Functions*, edited by H.Bateman and A.Erdélyi (Mc Graw-Hill, New York, 1955). Vol. 3.
- [120] S.Liu, J.Li, Q.Shen, Y.Cao, X.Guo, G.Zhang, C.Feng, J.Zhang, Z.Liu, M.L.Steigerwald, D.Xu, and C.Nuckolls, Angew. Chem. **48**, 4759 (2009).
- [121] P.L.Hernández-Martinez and A.O.Govorov, Phys. Rev. B **78**, 035314 (2008).
- [122] H.Hirori, K.Matsuda, and Y.Kanemitsu, Phys. Rev. B **78**, 113409 (2008).